Geophysics Open-File Report 8
Geoscience Department
New Mexico Tech
Socorro, NM 87801

SEISMIC FAULT MOTION AND SV WAVE SCREENING BY SHALLOW MAGMA BODIES IN THE VICINITY OF SOCORRO, NEW MEXICO

by

Paul J. Shuleski

Submitted in partial
fulfillment
of
the requirement
of
Geophysics 590
and the
Master's Degree Program
at
New Mexico Institute
of
Mining and Technology

October, 1976

The research described in this paper was sponsored jointly by the National Science Foundation (DES74-24187) and the State of New Mexico (Board of Educational Finance (BEF-6) and Energy Resource Board (ERB-75-300)).

ABSTRACT

A twelve month survey of microearthquake activity in the region around Socorro, New Mexico, was made using high magnification (5.6 million at 60 Hz) seismographs. In all, 69 Class A microearthquakes representing 340 separate events were used to construct a total of 14 composite fault-plane solutions. Grouping of microearthquakes for these composite solutions was based on geographic distribution and similarities in first motion and amplitude data at a given recording station.

Using SV amplitude data as well as first motion data, nine fairly well constrained fault-plane solutions were constructed. For these solutions, the fault motion was found to be dominantly normal.

A regional composite fault-plane solution was constructed using first motion data from 13 of the 14 composite solutions. The solution indicated dominantly normal faulting with a general N - S trend. This result is in good agreement with known tectonics of the Rio Grande rift.

For many earthquakes in the Socorro area, the amplitude of the SV wave was unusually small at one or more recording stations. Focal mechanism and high angle of incidence for the SV waves were found to be inadequate to explain all of the small SV amplitudes. An alternate explanation for many of the observations is that the SV waves were screened during passage through molten or partially molten rock. In all, 5 shallow magma bodies are proposed to explain the observed

screening of SV waves. Possible areas for the magma bodies are centered (1) 4.0 km NNE of Socorro within the Socorro basin, (2) 15.0 km SW of Socorro in the southern end of the La Jencia basin, (3) 4.0 km SW of Socorro beneath the Socorro Mountains, (4) 4.0 km SSW of Socorro within the Socorro basin, and (5) 12.0 km SSW of Socorro in the northern end of the Chupadera Mountains.

INTRODUCTION

The purpose of the study described in this report was to use data from microearthquakes in the Socorro region (1) to determine the type of faulting and thus the regional stress distribution, and (2) to locate possible shallow magma bodies (depths $<$ 10 km) by observing screening of SV waves. The results presented in this paper were obtained primarily from an analysis of composite fault-plane solutions that were constructed from recorded first motion and SV amplitude data.

PREVIOUS STUDIES

Socorro, New Mexico, is located within the Rio Grande rift, a major tectonic structure in southwestern U. S. The rift is characterized by normal faulting which has produced a series of basins and ranges aligned en echelon with a general north trend (see Figure 1). For a discussion of the rift and its boundaries in the vicinity of Socorro, see Chapin and Seager (1975) and/or Mott (1976).

Seismological investigations of microearthquake activity in the Socorro area began in 1960. Results of some of these studies will be briefly discussed below.

The majority of the seismic activity was found to be located to the south and west of Socorro (Sanford and Holmes, 1962; Sanford; 1963, Sanford and Long, 1965, Sanford et al., 1972; Mott, 1976). Sanford (1963) suggested this concentration of activity may be related to recent igneous intrusives or to current magmatic activity at depth.

Sanford et al. (1972) and Mott (1976) have shown little direct correlation exists between the distribution of microearthquakes and the known major faults within the rift. Analysis involving the length, displacements and ages of mapped fault scarps on the geomorphic surfaces indicate that the seismic activity in the Socorro region in not a recent development, but has existed for many thousands of years (Sanford et al., 1972).

Mott (1976) as part of his Independent Study constructed three composite fault-plane solutions for the Socorro area.

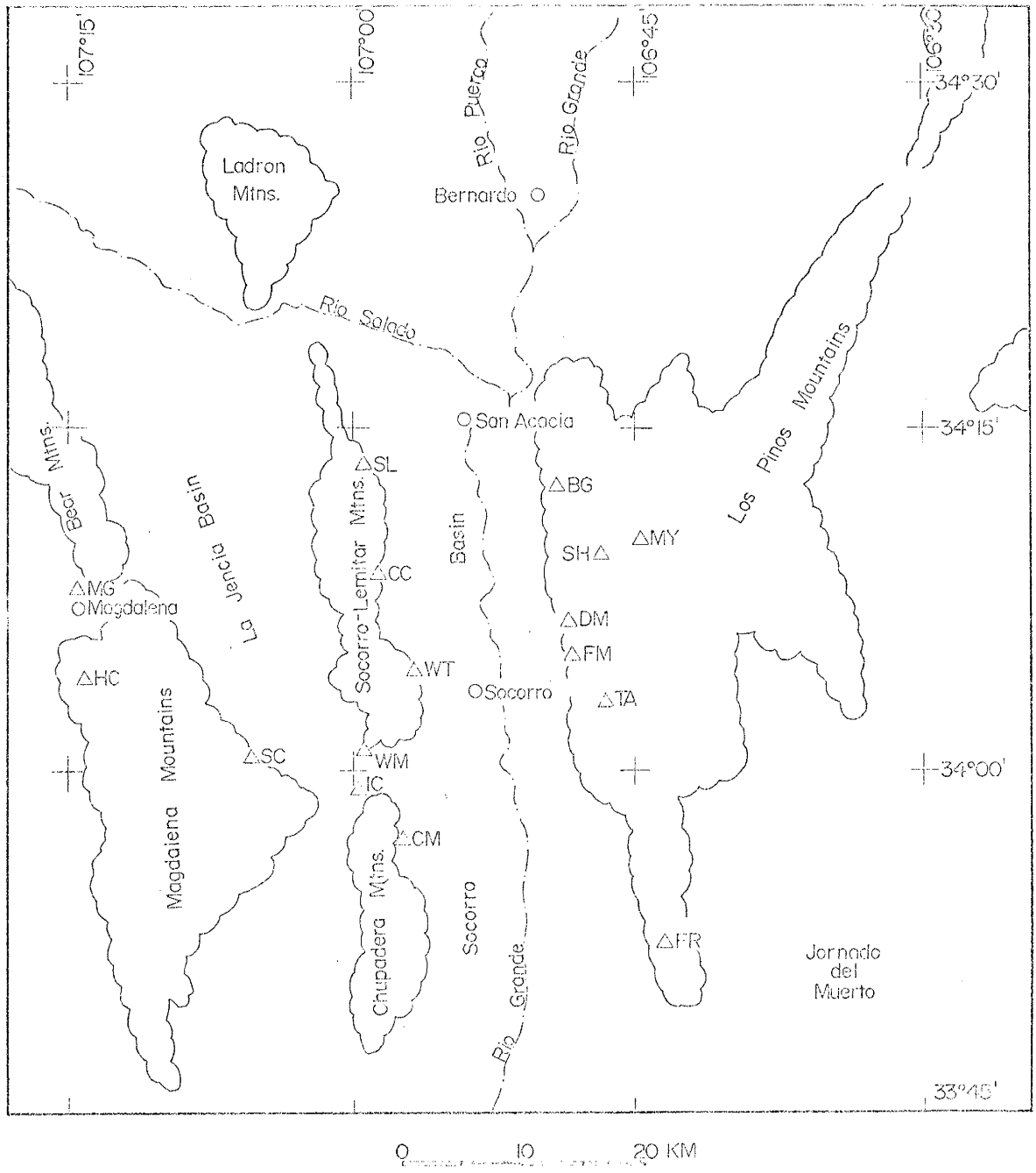

Figure 1 Map showing the basins and ranges of the Rio Grande rift near Socorro. Open triangles indicate locations of seismograph stations used in the study.

First motion data indicated normal faulting along a NNE-SSW trend. The solutions also indicated a near horizontal WNW-ESE trending axis of least principal (tensional) stress which is in agreement with the tectonics suggested for the rift.

A detailed gravity survey of the rift near Socorro (Sanford, 1968) indicated the Socorro and La Jencia basins to be asymmetrical in shape, particularly the Socorro basin. A narrow fault zone with large displacement borders the western edge of the latter graben structure. From its deepest point near the western margin, this structural basin was found to rise to the east by a combination of step-faulting and tilting.

A magma body at 18 km depth beneath Socorro was mapped by Sanford and Long (1965), Sanford et al. (1973) and Mott (1976) using reflected S_KS and S_KP phases. As presently mapped (Sanford et al., 1976) the magma body occurs beneath a minimum of 1000 km^2 of the central part of the rift at depths of 18 km to 21 km. The general shape of the body is that of an elongated laccolith with a NNE-SSW trend.

INSTRUMENTATION

Microearthquake data used in the study was recorded by four to six Sprengnether MEQ-800 portable seismic systems. Each system consisted of either a Willmore (1.5 Hz natural frequency) or a Mark Products L4-C (1.0 Hz natural frequency) vertical seismometer, a quartz-crystal timing system, a gain stable amplifier, and a smoked paper recorder which operated at a recording speed of 120 mm/minute. Gain settings could be varied through a range of 60db to 120db in 6db increments depending on the background noise conditions. Filtering of low and high frequency signals was also possible with this system, although under optimum operation conditions no filtering was used.

The magnification response of the MEQ-800 seismic system is shown in Figure 2 for standard operating conditions. The magnification peaks near 5.4×10^6 at approximately 60 Hz, making the MEQ-800 seismic system an excellent instrument for studying microearthquakes which are characterized by high frequencies and small ground displacements.

Clocks of all the systems were synchronized to WWVB-UST at the start of each recording "week" (Monday through Friday). Drifts were found to have a range of 0.00 to 0.30 seconds for the four day interval and were assumed to occur linearly over that time period.

For the time period of May 20, 1975 to May 25, 1976, a total of twenty temporary seismograph stations were occupied in the Socorro region. Stations for the array were chosen

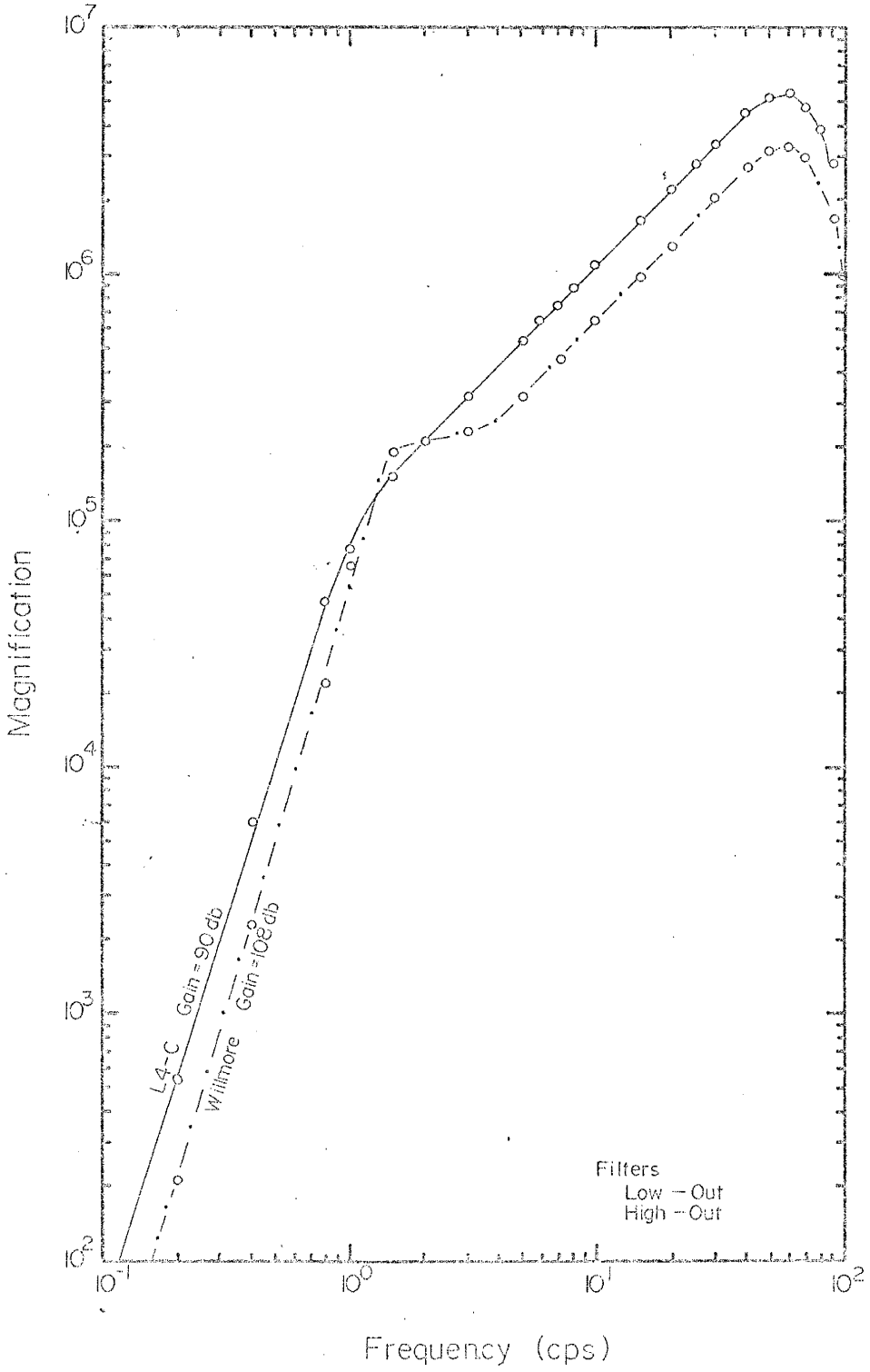

Figure 2 Magnification curves of MEQ-800 seismic unit with either L-4C or Willmore geophones at optimum gain settings of 90db and 108db, respectively.

on the basis of (1) the particular geographic area to be studied and (2) those stations which gave the optimum azimuthal coverage of that area. Locations for 16 of the seismograph stations are shown in Figure 3(a) and location parameters for each station are listed in Table 1.

Table 1

Portable Seismograph Station Locations

Station	Latitude	Longitude	Elevation(M)
BG	34.2068	106.8205	1516
CC	34.1442	106.9812	1649
CM	33.9501	106.9576	1640
CU	34.1573	106.7785	1585
DM	34.1075	106.8079	1536
FM	34.0829	106.8047	1537
FR	33.8747	106.7270	1558
HC	34.0658	107.2361	2240
IC	33.9870	106.9967	1730
LAD	34.4583	107.0375	1768
LPM	34.3076	106.6336	1737
MG	34.1305	107.2425	2024
MY	34.1667	106.7459	1645
NJ	33.9924	106.6253	1644
SC	34.0100	107.0894	2073
SH	34.1570	106.7802	1577
SL	34.2234	106.9910	1615
TA	34.0498	106.7751	1558
WM	34.0120	106.9929	1673
WT	34.0722	106.9459	1555

LOCATION OF MICROEARTHQUAKES

Procedure

Two computer programs were used in determining microearthquake epicenters. A graphical plot, depicting the intersection of hemispheres, was initially used. Later an iterative numerical method was adopted. For the same data, both methods were found to give comparable results.

In determining initial origin times of microearthquakes for both programs, recorded P and S wave arrival times were used. Origin time was determined from Wadati diagrams or calculated from the following equation

$$\text{Origin Time} = P - \frac{S - P}{V_p/V_s - 1.0} , \qquad (1)$$

where P and S are the arrival times and V_p and V_s are the velocities of the P and S waves. Assuming a value of 0.25 for Poisson's ratio, V_p/V_s reduced to $\sqrt{3}$ and the origin time equation then became

$$\text{Origin Time} = P - 1.3666(S - P) . \qquad (2)$$

In both location programs, it was assumed that the crust in the Socorro region was a homogeneous and isotropic half-space with a P wave velocity of 5.8 km/sec.

In this study, only Class A microearthquake locations were used. Class A locations are defined as hypocenters which (1) have been determined by four or more seismic stations, (2) have epicenters within the seismic station array, and (3) have estimated relative errors of ± 0.5 km in geographic location and ± 2.0 km in depth (Mott, 1976).

Geographic Distribution

Epicenters for 91 Class A microearthquakes are shown in Figure 3(a). The origin time, event number, and location parameters of each Class A epicenter are given in Table 2. Table 2 also lists the number of microearthquakes (NQ) occurring at each hypocenter. Swarms, i.e. multiple events from the same focus within a short time interval (6 - 12 hours), have been observed in the Socorro area. Thus the 91 Class A hypocenters given in Table 2 are the locations for a total of 448 separate events.

Depths of focus were found to range from 0.0 km to 14.0 km and 63% of all the events occurred from 6.0 km to 9.0 km beneath the surface.

In general the microearthquakes occur in a diffuse band extending along the axis of the Rio Grande rift (Figure 3(a). However, 53% of the seismic activity has been to the west and south of Socorro along (1) the southwestern edge of Socorro Mountain, (2) the southern end of the La Jencia basin, and (3) the northern border of the Chupadera Mountains. A more diffuse pattern of activity was observed to occur within the Socorro basin. Previous studies by Sanford and Holmes (1962), Sanford (1963), Sanford and Long (1965), Sanford et al. (1972) and Nott (1976) have also shown a similar distribution of epicenters.

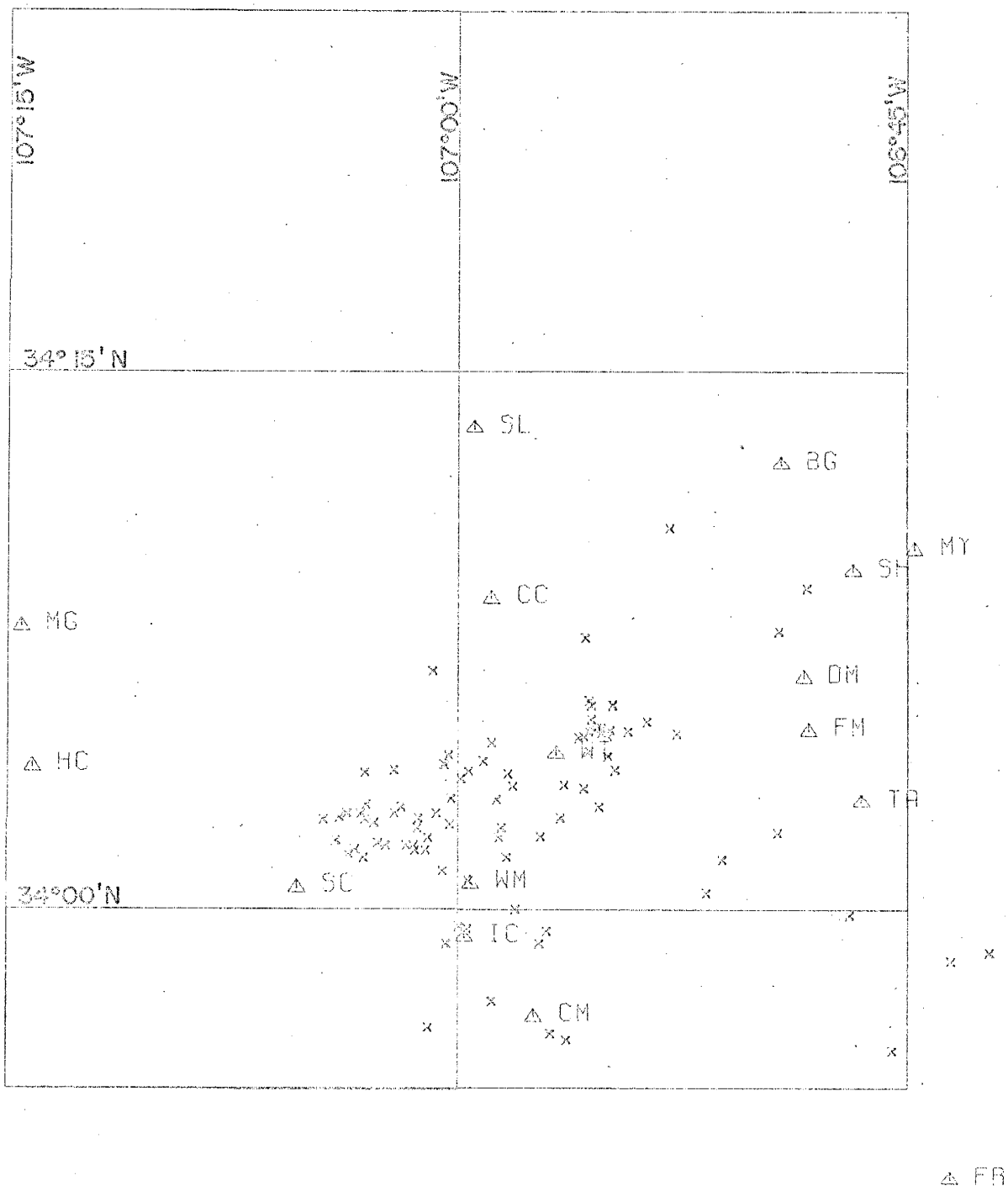

Figure 3(a) Geographic distribution of Class A microearthquakes in the Socorro region for the time period of May 20, 1975 to May 25, 1976. Epicenters are indicated by x's; recording stations are shown as open triangles.

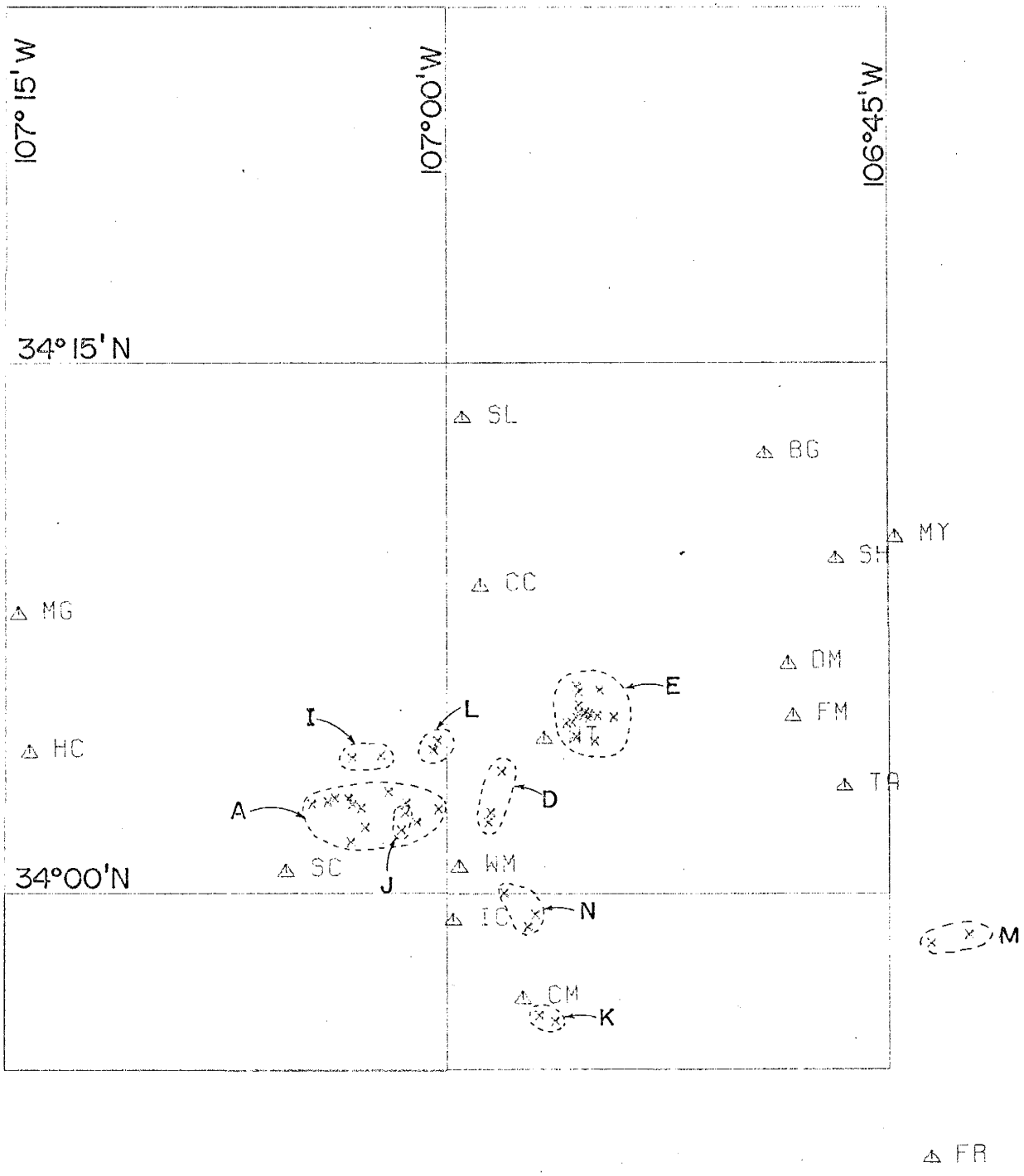

Figure 3(b) Map showing the grouping of Class A events used in the construction of composite fault-plane solutions.

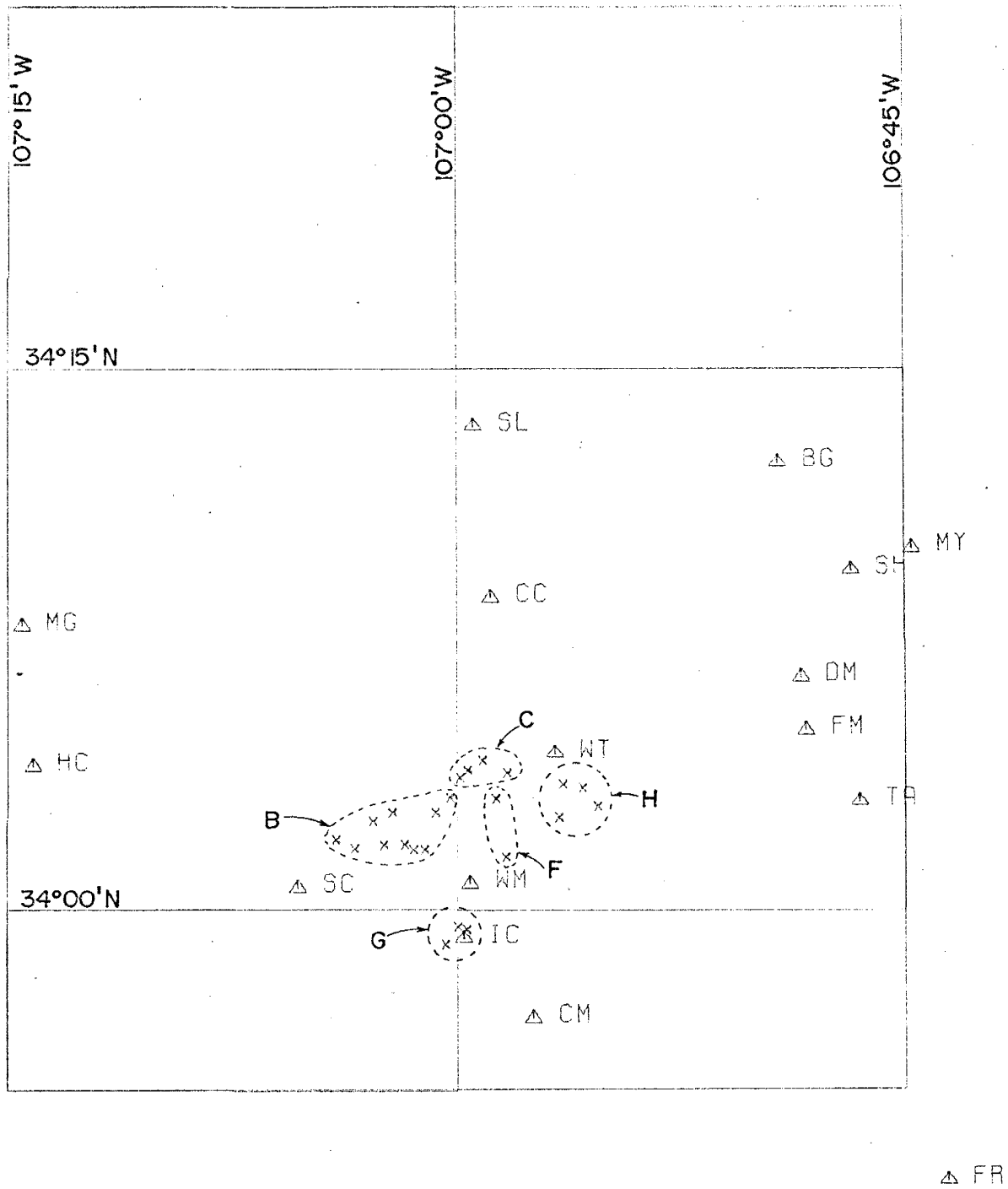

Figure 3(c) Map showing the grouping of Class A events used in the construction of composite fault-plane solutions.

Table 2

Location of Class A Microearthquakes

Date	Event #*	Origin Time	Latitude	Longitude	Depth**	NQ***
5-20-75	57	04:25:09.20	33.9427	106.9488	4.97	2
5-20-75	1	17:10:01.60	34.0946	106.9144	9.35	1
5-22-75	2	10:27:08.50	34.0815	106.8794	3.95	1
5-22-75	13	11:36:29.03	33.9397	106.9395	4.75	1
5-26-75	3	23:45:51.30	34.0775	106.9810	7.99	1
5-29-75	4	07:14:12.12	33.9452	107.0168	9.58	1
6-03-75	5	02:45:09.60	34.0826	106.9062	3.34	12
6-03-75	37	04:48:17.80	34.0844	106.9204	9.29	1
6-03-75	12	15:10:15.60	34.0301	107.0296	10.34	1
6-16-75	6	23:43:21.11	34.0276	107.0242	10.80	1
6-17-75	7	15:30:45.14	34.0647	106.9129	7.35	1
6-17-75	8	18:50:33.31	34.0640	107.0520	10.60	2
6-26-75	9	02:56:45.11	34.0547	107.0365	6.11	2
7-01-75	48	13:35:58.50	34.0301	107.0408	9.96	1
7-09-75	50	02:12:24.80	34.0562	106.9302	6.11	6
7-09-75	17	09:16:47.97	34.0804	106.9167	8.67	2
7-23-75	19	14:56:41.62	34.0281	107.0576	13.00	3
7-24-75	51	04:23:14.30	34.0646	106.9940	5.18	1
7-30-75	52	21:44:42.10	34.0848	106.9223	8.23	1
8-05-75	14	02:26:02.50	34.0335	106.9772	7.58	8
8-05-75	16	04:17:20.92	34.0379	106.9758	7.78	1

* - Events 1-57 taken after Mott 1976, 1A-34A after Rinehart

** - Datum taken as 1.666km above sea level

*** - Number of microearthquakes at the same focus

Table 3 Continued

Date	Event #*	Origin Time	Latitude	Longitude	Depth**	NQ***
8-08-75	10	10:53:58.00	34.0837	106.9233	6.69	2
8-08-75	21	10:57:22.59	34.0796	106.9329	6.80	6
8-12-75	18	03:59:36.10	33.9574	106.9812	3.95	1
8-12-75	20	07:09:11.15	34.0357	106.8225	0.00	1
8-12-75	11	15:25:28.30	34.0513	106.9785	8.78	1
8-13-75	15	05:19:18.20	34.0823	106.9207	8.15	27
8-13-75	25	07:39:18.40	34.0826	106.9274	7.92	1
8-13-75	27	11:22:26.90	34.0245	106.9731	9.05	1
8-15-75	56	06:36:45.80	34.0871	106.8957	7.28	2
8-19-75	24	08:11:46.60	34.0580	106.9409	10.93	2
8-19-75	22	10:00:07.20	33.9922	107.0000	10.88	1
8-19-75	55	20:10:22.60	34.0971	106.9276	9.16	4
8-20-75	23	05:22:19.70	34.0882	106.9261	10.05	15
8-20-75	26	12:20:52.35	34.0833	106.9153	7.01	2
8-20-75	28	15:29:36.60	34.0848	106.9261	6.94	2
8-20-75	29	21:59:44.30	34.0947	106.9261	8.91	6
8-21-75	38	03:44:48.70	34.0407	107.0470	9.51	1
8-21-75	30	19:04:06.50	34.0575	106.9692	7.54	10
8-25-75	32	19:37:41.10	34.0714	106.9167	6.73	5
8-26-75	31	08:40:15.40	34.0480	106.9220	9.40	12
8-28-75	33	01:26:02.50	34.1264	106.9296	2.87	5
8-29-75	35	08:52:18.80	34.0737	106.9271	7.19	20
9-16-75	45	13:30:52.55	34.0804	106.9301	6.66	1
9-19-75	42	08:42:57.21	34.0234	106.8539	5.52	1

Table 2 Continued

Date	Event #*	Origin Time	Latitude	Longitude	Depth**	NQ***
9-24-75	44	02:17:09.30	34.0954	106.9140	7.25	7
10-29-75	41	07:21:35.35	34.0609	106.9987	3.87	4
10-29-75	53	20:50:49.60	34.0134	106.9940	4.76	2
10-30-75	34	07:09:39.20	34.0335	107.0168	5.59	1
10-31-75	54	04:02:15.27	33.9345	106.7589	9.59	1
11-04-75	47	16:30:12.10	34.0491	107.0517	6.24	31
11-05-75	39	02:40:10.50	33.9973	106.7823	9.83	1
11-05-75	36	14:35:05.50	34.0402	107.0475	7.60	22
11-05-75	43	22:28:26.70	34.0424	107.0228	4.45	19
11-06-75	40	09:33:59.20	34.0396	107.0047	7.98	2
11-06-75	49	11:05:48.30	34.0078	106.8629	7.97	1
11-07-75	46	08:27:36.10	34.0480	107.0323	7.09	25
1-21-76	8A	05:34:40.93	34.0628	106.9721	5.55	6
1-21-76	7A	14:18:28.75	33.9839	106.9551	5.66	2
1-22-76	9A	16:05:11.03	34.0452	107.0359	10.79	3
1-22-76	11A	22:14:30.50	34.0337	106.9536	0.00	2
1-22-76	12A	22:50:07.60	34.1770	106.8830	0.00	1
1-23-76	10A	02:53:33.68	34.0208	107.0180	5.67	1
1-27-76	13A	08:37:44.73	34.1290	106.8220	9.07	37
1-27-76	14A	10:05:27.07	34.1490	106.8060	9.85	1
1-29-76	15A	15:06:40.47	34.0000	106.9680	5.46	10
1-30-76	16A	13:56:23.95	34.0690	106.9861	5.27	3
2-17-76	1A	06:17:49.59	34.0450	107.0620	10.05	1
2-17-76	17A	23:19:38.61	34.1110	107.0140	9.77	3
2-17-76	18A	17:34:05.13	34.0517	107.0045	10.89	2

Table 2 Continued

Date	Event #*	Origin Time	Latitude	Longitude	Depth**	NQ***
2-18-76	6A	05:44:55.76	34.0237	107.0525	10.49	1
2-18-76	2A	09:13:30.54	34.0183	107.0087	4.95	1
2-18-76	5A	23:25:35.22	34.0420	107.0520	6.37	1
2-19-76	4A	00:08:36.77	34.0261	107.0612	10.68	1
2-20-76	3A	12:51:45.10	34.0310	107.0450	13.39	2
3-18-76	20A	14:45:16.00	33.9760	106.7260	9.89	11
3-18-76	19A	18:34:49.95	34.0420	107.0750	10.67	1
3-23-76	23A	12:50:26.35	33.9800	106.7050	0.00	1
3-25-76	21A	10:50:54.65	34.0425	106.9435	5.71	1
3-25-76	22A	13:57:02.90	34.0430	107.0660	9.10	2
4-13-76	31A	09:54:40.73	34.0720	107.0050	5.87	3
4-13-76	24A	11:41:25.73	34.0450	107.0540	7.07	2
4-13-76	25A	11:58:34.65	33.9900	106.9510	6.62	5
4-13-76	26A	13:31:59.42	33.9840	107.0067	8.94	1
4-13-76	28A	23:15:15.00	34.0300	107.0250	6.13	1
4-14-76	29A	01:50:28.91	33.9910	106.9950	10.24	3
4-15-76	27A	08:45:52.70	34.0680	107.0080	6.74	17
4-16-76	32A	05:34:38.85	34.0380	107.0230	6.07	1
4-16-76	30A	09:33:43.03	34.0670	107.0070	6.20	20
5-25-76	33A	03:08:17.00	34.0452	107.0120	2.79	2
5-25-76	34A	08:11:38.95	34.0322	107.0682	9.41	1

FAULT-PLANE SOLUTIONS

Elastic Rebound Theory

The focal mechanisms of earthquakes have long been investigated by seismologists. John Milne in 1891 was the first to recognize fault displacement as a possible source of seismic energy (Richter 1958). After the 1906 San Francisco earthquake Reid (1910) established the fault-earthquake relationship based on geodetic measurements. From these observations Reid was able to develop the elastic rebound theory.

According to the theory, the source of the energy released from earthquakes is the elastic strain energy stored within the crustal blocks. If no pre-existing faults are present, this stored energy is released when the shear stress exceeds the strength of the rock and fracture occurs. If the stored energy is allowed to accumulate along a pre-existing fault, slippage will occur when the shear stress exceeds the frictional resistance of the rock. Such displacements along new fractures or pre-existing faults release the stored elastic strain energy. Some of the energy released is expended in heat and deformation of the rock in the vicinity of the source. The remaining energy is propagated away from the source as elastic waves, both body and surface waves.

Reid's theory offers a model of an earthquake source, but an accurate physical mechanism is still unclear. Consequently, mathematical models have been developed to fit

the data. The simplest model is that of a point source from which the double-couple model was derived (Honda 1962). The double-couple model is shown in Figure 4. The model is equivalent to two orthogonal principal stresses orientated ±45 degrees to the fault-plane.

Fault-Plane Solution Theory

When seismic waves pass through the earth which has a heterogenous composition and structure, the relatively simple disturbance generated at the focus becomes quite complex at a particular recording station. However, the initial particle motion of the P and S waves will remain unchanged by passage through the earth because these seismic waves are transmitted in the direction of and transverse to the direction of propagation. Because P waves travel faster than S waves they will always be recorded first at the seismograph. Byerly (1938) developed a technique for using the observation of P wave first motions to determine the source mechanisms of earthquakes. Later Gutenberg (1941), Byerly (1955), Hodgson and Milne (1951), and others refined the procedure.

Figure 5 is a model of a normal fault having pure dip-slip movement. In the neighborhood of the focus, compressional motions are produced in two quadrants (solid ray paths), and dilatational first motions in the other two quadrants (dashed ray paths). No change in the direction of first motion with distance is to be expected, and thus all stations located at the end of solid ray paths should

DOUBLE COUPLE MODEL

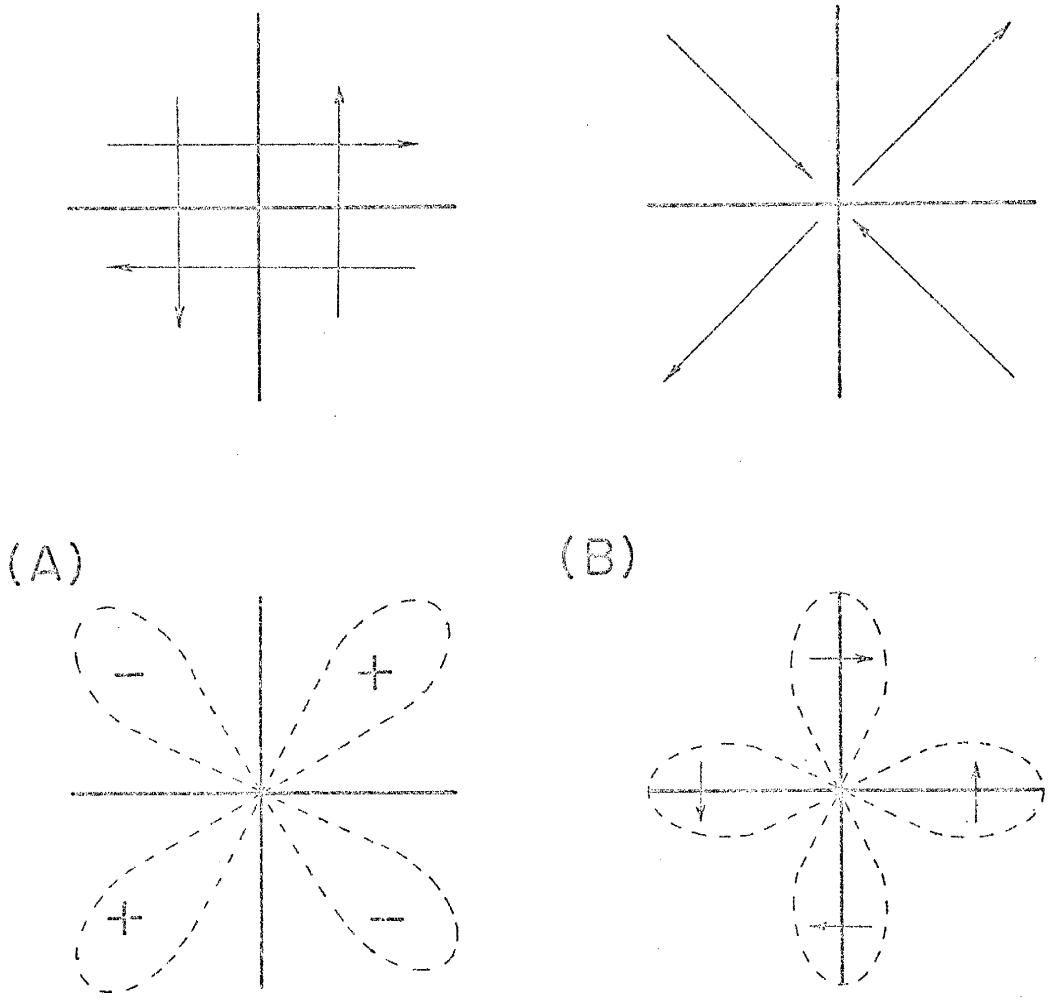

Figure 4 Double couple point source model showing the (A) P wave radiation pattern and (B) the S wave radiation pattern (+ indicates compressions, − indicates dilatations, and ⟶ indicates the direction of shear motion).

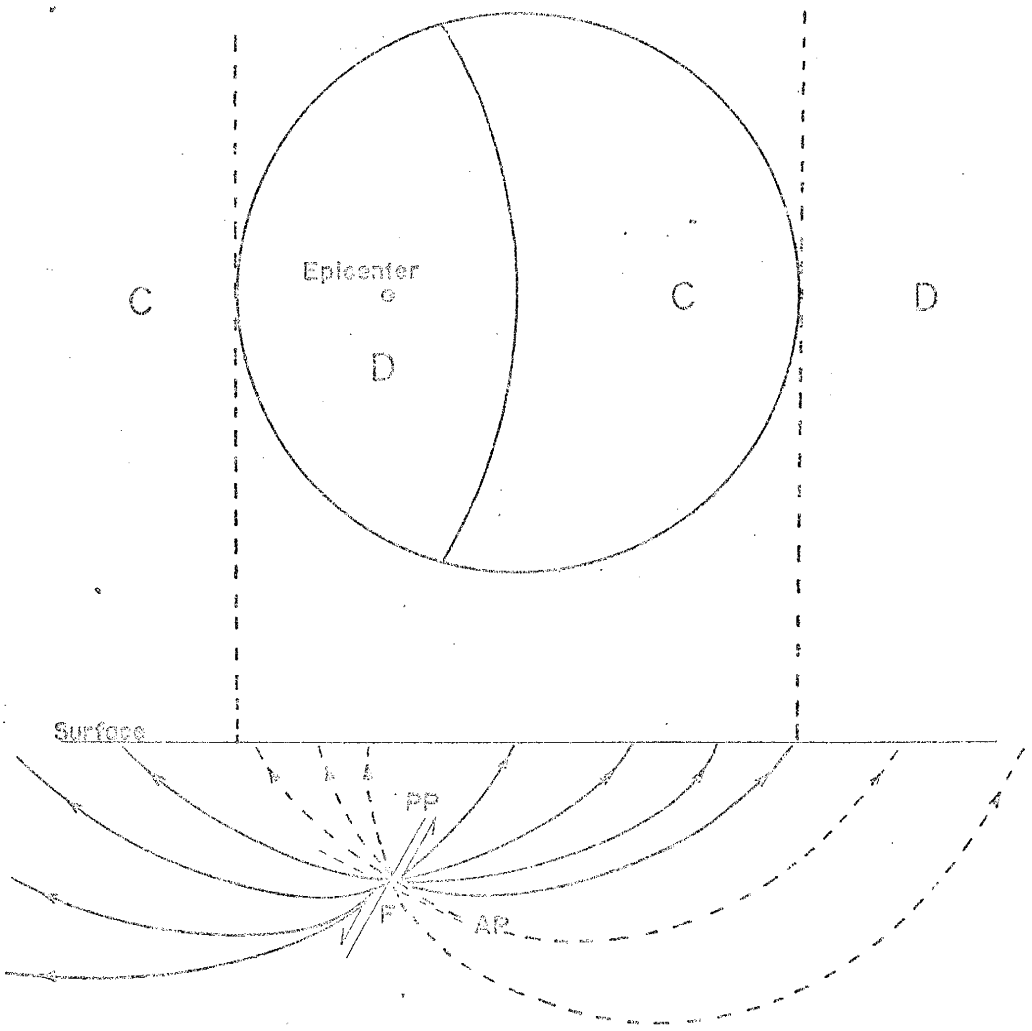

Figure 5 Distribution of compressions (C) and dilatations (D) at the earth's surface for a normal fault having pure dip-slip movement. Ray paths for the compressional first arrivals are shown as solid lines, ray paths for the dilatational first arrivals as dashed lines. The focus (F), fault-plane (FP) and auxiliary-plane (AP) are also shown.

record on vertical seismometers an initial impulse directed upward. For stations at the end of dashed ray paths, the first motions should be reversed.

The plane along which fault displacement occurs is termed the "fault-plane" and the plane orientated perpendicular to it is termed the "auxiliary-plane". Theoretically these are both planes along which no P wave motion can occur, i.e. they are nodal planes. By observing the initial P wave motion at a number of seismograph stations distributed over the surface about the focus, the orientation of the fault-plane and auxiliary-plane may be determined.

In this study, the stereographic method of presenting first motion data was used Stauder (1962), Herrmann (1975). (For a complete description of the stereographic projection method, see Ramsay (1967) or Ragan (1973).) In this method, the focus of an earthquake is surrounded by a hypothetical sphere called the "focal sphere"; this focal sphere being the unit sphere in stereographic projection. The position at which the rays to the recording stations pass through the focal sphere can be determined. The resulting distribution of initial motions can determine the orientation of the fault and auxiliary planes. It should be noted that only one hemisphere of the focal sphere is used in stereographic projection. If most of the recording stations used in the analysis are at large distances from the focus, the lower hemisphere is used. However, for short distances, the upper hemisphere projection is commonly used.

Initially, the stereographic projection method des-

cribed above was used primarily for large shocks. Gutenberg (1941) showed, however, that the above theory could also be applied to local shocks. If one assumes a similarity of focal mechanisms for a number of individual local shocks within a given region, the initial motion data can be combined to give what is called "a composite fault-plane solution". Stauder and Ryall (1962) and Hadly and Combs (1974) have successfully used this technique for microearthquake studies of central Nevada and southern California, respectively.

Procedure

A total of 14 composite fault-plane solutions were constructed. Data from 69 of the 91 Class A events were incorporated in these solutions. Grouping of shocks for the composite fault-plane solutions (see Figures 3(b) and 3(c)) was on the geographic distribution and similarities in first motion and amplitude data at a given station.

The observed first motions at a station were plotted on a Wulff stereonet at the azimuth (AZ) and the angle of incidence (i) of the station with respect to the focus. The angle of incidence is given by:

$$i = \cos^{-1}(h/r) \qquad (3)$$

where,

h: is the depth of focus

r: is the linear distance between the focus and the station .

Because a homogeneous half-space was assumed for the crustal model, rays could be assumed to follow straight ray paths from the focus to a station.

After the first motion data was plotted on the stereonet, the P nodal planes were drawn such that (a) the nodal planes separated compressions from dilatations and (b) the nodal planes were orthogonal to each other. The resulting diagram shows two perpendicular planes, the fault-plane and auxiliary-plane, separating compressions from dilatations. The ambiguity of the resulting solution is that the fault-plane cannot be distinguished from the auxiliary-plane without other geological and/or geophysical information.

The fault-plane (F) was chosen as the P nodal plane having the greatest dip. For normal faulting this choice was justifiable. Geological field observations of known faults as well as theoretical studies have shown that normal faults have dips of approximately 60 - 65 degrees. However, no similar geological justifications hold for strike-slip and reverse faulting and here the choice was purely arbitrary.

Interpretation of Fault-Plane Solutions

Three fundamental types of faulting may be interpreted from fault-plane solutions:

(a) normal faulting

(b) reverse faulting

(c) strike-slip faulting

Each of the three types of faulting generate different distributions of first motions on the stereonet (Figure 6). For normal and reverse faults, the stereonet is divided into three sections of dilatations and compressions, where as strike-slip faults show a clear quadrantal pattern. Combinations of these three types are possible and are commonly observed in practice.

In analyzing fault-plane solutions, five axes, the P, T, B, X, and Y (Figure 6) are commonly used. Their physical and geometrical definitions are given below:

P: the axis of greatest principal stress orientated ±45 degrees from the fault-plane. It is always located in a region of dilatations

T: the axis of least principal stress orientated ±45 degrees to the fault-plane. It is always located in a region of compressions

B: the axis of intermediate stress (null axis) located at the intersection of the fault-plane and auxiliary-plane. This axis is normal to the direction of motion

X: is the direction of motion along the fault-plane and is normal to the auxiliary-plane

Y: the node of the fault-plane. It is normal to the fault-plane and lies in the

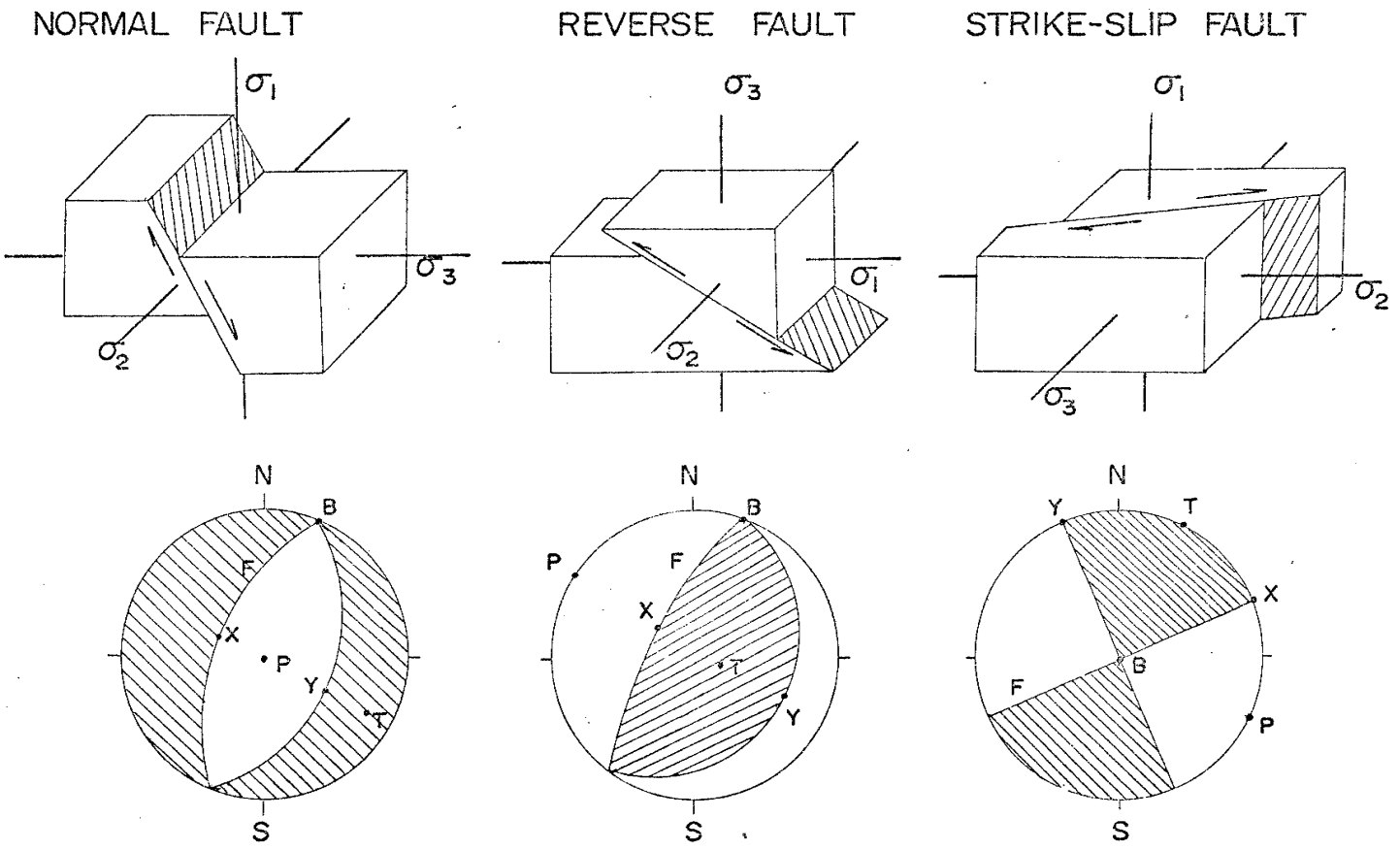

Figure 6 Block diagram of the three types of faulting and the corresponding fault-plane solutions. σ1, σ2, σ3 are the principal stresses where σ1 > σ2 > σ3. The fault-plane is indicated by F in the diagram; a description of the P, T, B, X, and Y axes is given in the text.

auxiliary-plane .

The axes P, T, B and X, Y, B form two orthogonal systems rotated about the B axis by an angle of ±45 degrees to each other.

FAULT MOTION FROM FOCAL PLANE SOLUTIONS

Focal Plane Solutions Based Only on Initial P Motions

In this section each of the 14 composite fault-plane solutions is discussed separately. The solutions are presented in the order of the best to the least constrained. The azimuth and plunge for the principal axes of each solution are listed in Table 3. Table 4 lists the observational data for each composite solution. The data tabulated include the event number from Table 2, station, type of first motion, the amplitude ratio W_p/W_{sv}, azimuth and angle of incidence.

The seven best constrained solutions (Solutions A, B, D, F, G, H, N) are discussed first. For each of these solutions, shown in Figures 7 through 13, two extreme orientations of the P nodal planes were determined on the basis of the observed first motion data. On the stereographic projections, the maximum clockwise orientation for the P nodal planes is shown by solid lines and the axes for this solution by P_1, T_1, B_1, X_1, Y_1, and the maximum counterclockwise orientation for the P nodal planes is shown by dashed lines and its axes by P_2, T_2, B_2, X_2, Y_2. For each solution, the P nodal plane with the steepest dip was selected as the fault-plane.

Solution A (Figure 7) is based on data from 12 microearthquakes with an average focal depth of 8.3 km located in the southern La Jencia basin (Figure 3(b)). Both solutions 1 and 2 indicate dominantly normal faulting on a plane

striking N 24° E and having a dip of 66° E and 68° E respectively. The orientations of the fault-plane and auxiliary-plane for both solutions were fairly well constrained by the first motion data.

Solution H (Figure 8) is based on data from 4 micro-earthquakes with an average focal depth of 8.0 km located along the eastern margin of Socorro Mountain (Figure 3(c)). Solution 1 indicates dominantly normal faulting on a plane striking N 10° W and dipping 54° E. Solution 2 indicates a combination of normal faulting and right-hand strike-slip faulting on a plane striking N 10° W and dipping 54° E. The orientation of the fault-plane, the nodal plane with greatest dip, in both solutions, was well constrained by the first motion data.

Solution N (Figure 9) is based on data from 3 micro-earthquakes with an average focal depth of 5.9 km located on the northern end of the Chupadera Mountains (Figure 3(b)). Solution 1 indicates dominantly normal faulting on a plane striking N 12° W and dipping 54° E. Solution 2 indicates dominantly normal faulting on a plane striking N 28° W and dipping 60° E. The P nodal planes of both solutions were well constrained by the first motion data.

Solution D (Figure 10) is based on data from 3 micro-earthquakes with an average focal depth of 7.6 km located on the southwestern margin of the Socorro Mountains (Figure 3(b)). Solution 1 indicates dominantly normal faulting on a plane striking N 12° E and dipping 64° E. Solution 2 indicates dominantly normal faulting on a plane striking N 13° W

and dipping 62° E. The orientation of the auxiliary-planes for both solutions was fairly well constrained by the first motions observed at station FM.

Solution F (Figure 11) is based on data from 2 micro-earthquakes with an average focal depth of 8.9 km located on the southwestern margin of the Socorro Mountains (Figure 3(c)). Solution 1 indicates a combination of normal faulting and left-hand strike-slip faulting on a plane striking N 15° E and dipping 60° E. Solution 2 indicates dominantly normal faulting on a plane striking N 45° W and dipping 46° NE The auxiliary-plane for both solutions 1 and 2 was fairly well constrained by the first motion data.

Solution B (Figure 12) is based on data from 10 micro-earthquakes with an average focal depth of 9.3 km located in the southern La Jencia basin (Figure 3(c)). Solution 1 indicates a combination of normal faulting and right-hand strike-slip faulting on a plane striking N 20° W and dipping 63° W. Solution 2 indicates dominantly normal faulting on a plane striking N 20° W and dipping 63° W. The fault-plane of both solutions 1 and 2 was well constrained by the first motion data.

Solution G (Figure 13) is based on data from 3 micro-earthquakes with an average focal depth of 10.0 km located in the northern Chupadera Mountains (Figure 3(c)). Solution 1 indicates a combination of normal faulting and left-hand strike-slip faulting on a plane striking N 22° E and dipping 56° E. Solution 2 indicates dominantly left-hand strike-slip faulting on a plane striking N 01° E and dipping 80° E.

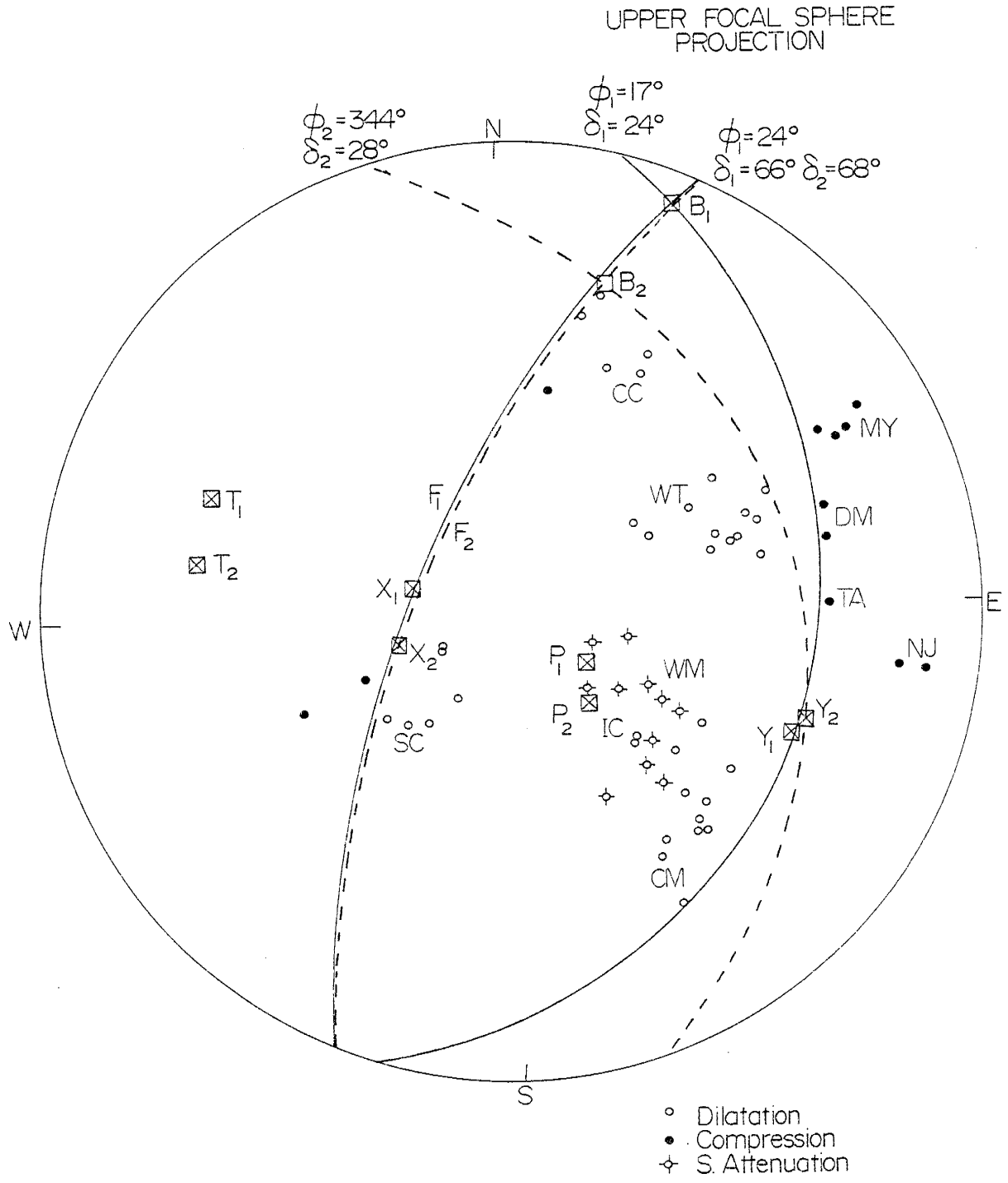

Figure 7 Composite fault-plane Solution A based on observed first motion data. The maximum clockwise (solid line) and counterclockwise (dashed line) orientations of the P nodal planes are shown.

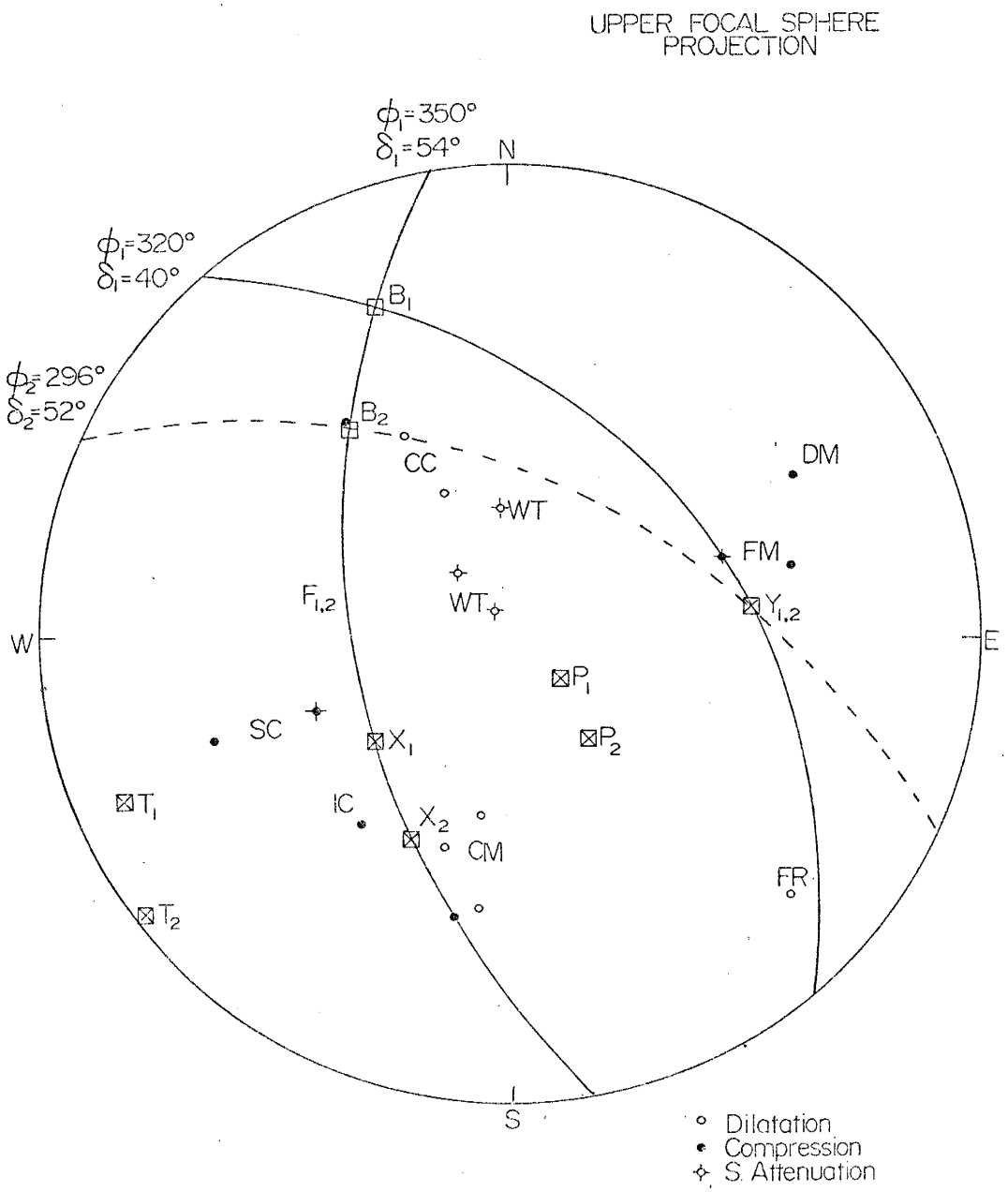

Figure 8 Composite fault-plane Solution H based on observed first motion data. The maximum clockwise (solid line) and counterclockwise (dashed line) orientations of the P nodal planes are shown.

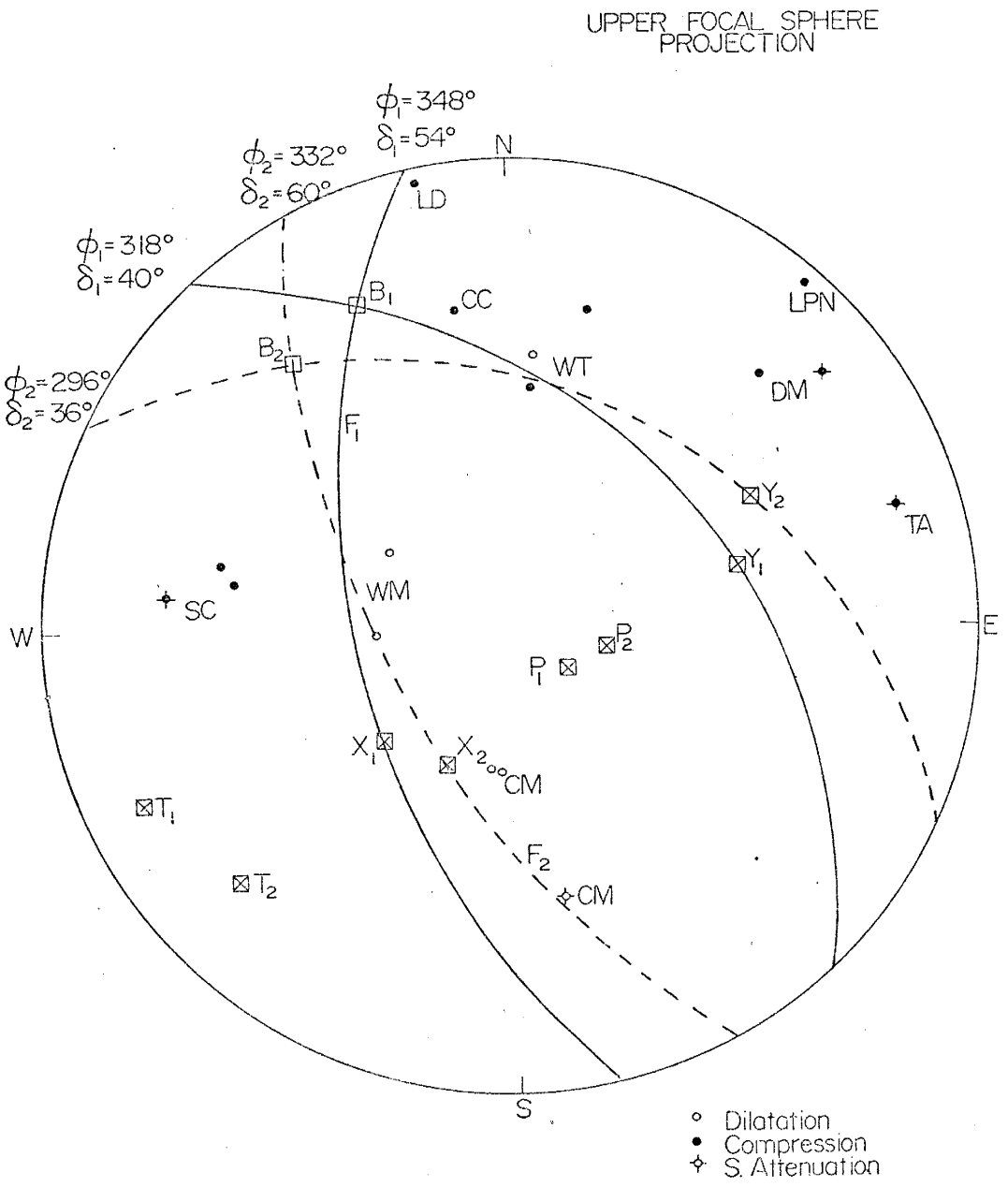

Figure 9 Composite fault-plane Solution N based on observed first motion data. The maximum clockwise (solid line) and counterclockwise (dashed line) orientations of the P nodal planes are shown.

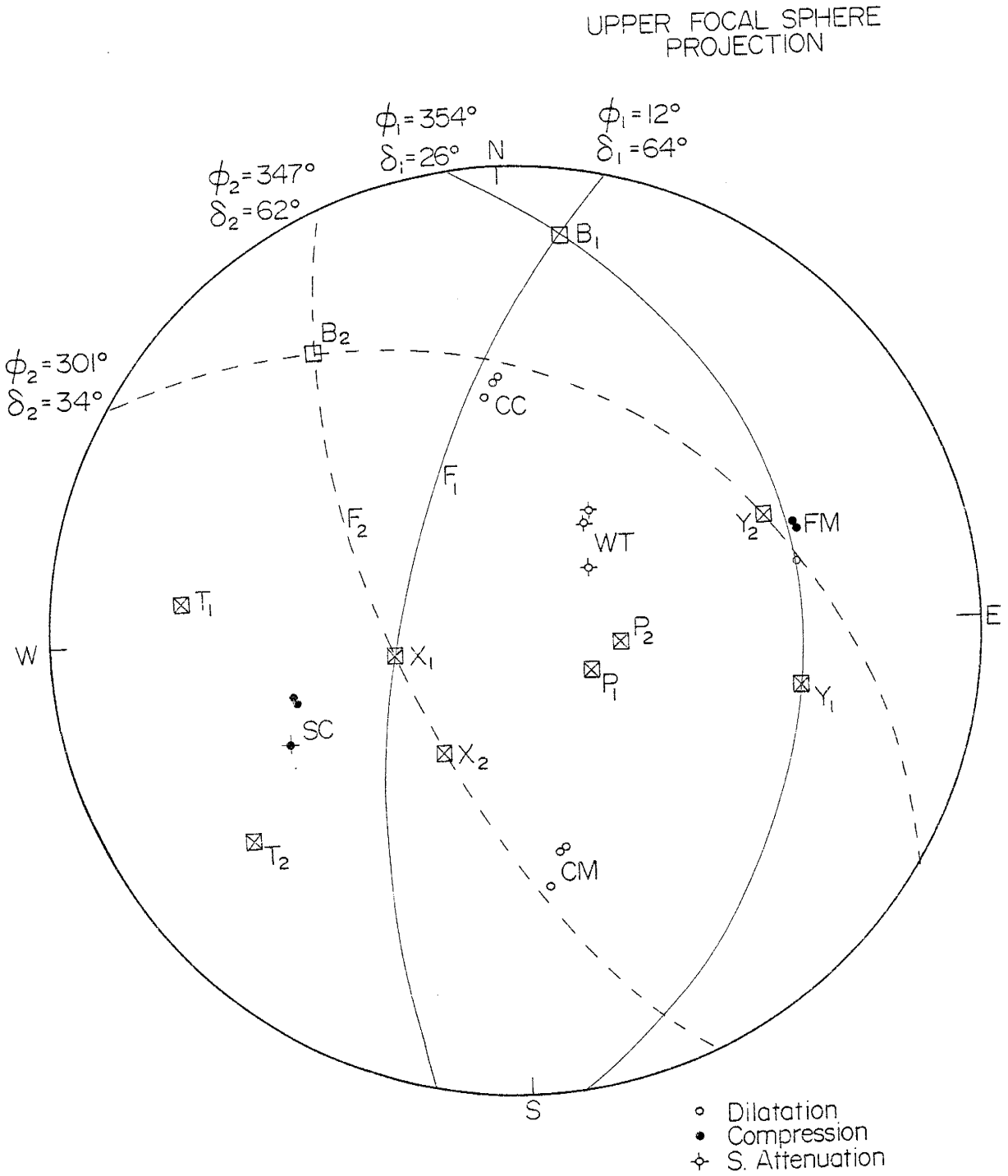

Figure 10 Composite fault-plane Solution D based on observed first motion data. The maximum clockwise (solid line) and counterclockwise (dashed line) orientations of the P nodal planes are shown.

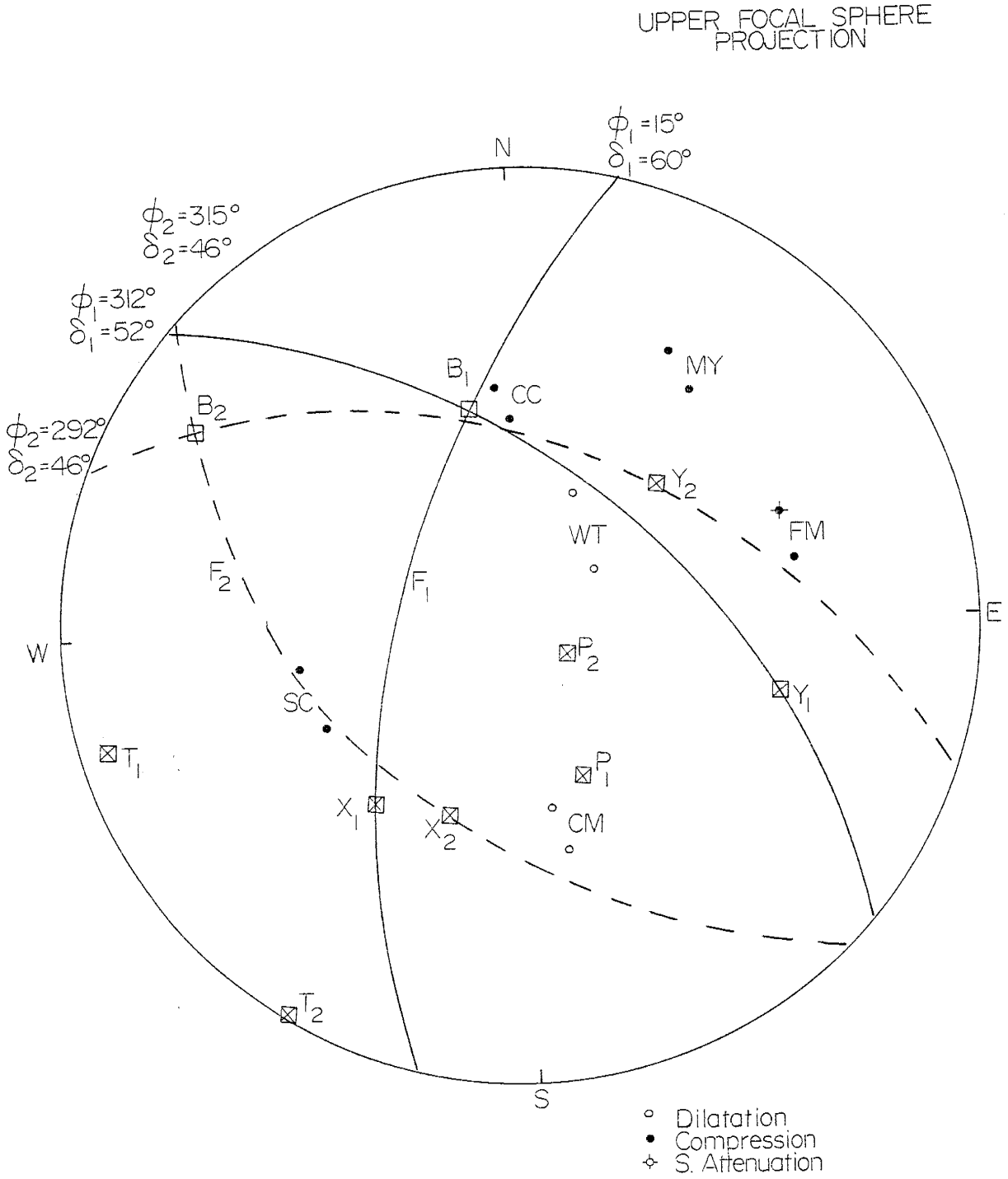

Figure 11 Composite fault-plane Solution F based on observed first motion data. The maximum clockwise (solid line) and counterclockwise (dashed line) orientations of the P nodal planes are shown.

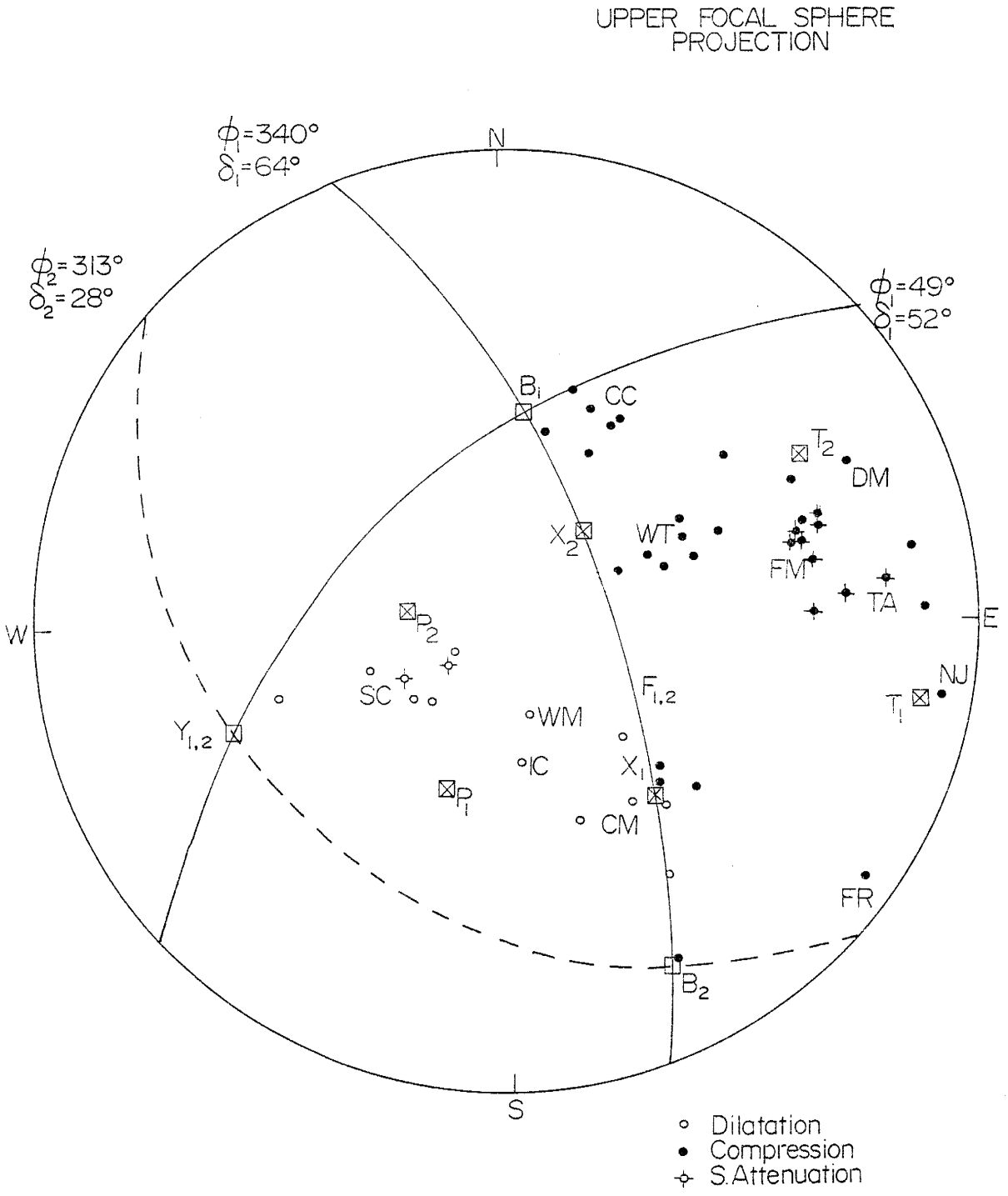

Figure 12. Composite fault-plane Solution B based on observed first motion data. The maximum clockwise (solid line) and counterclockwise (dashed line) orientations of the P nodal planes are shown.

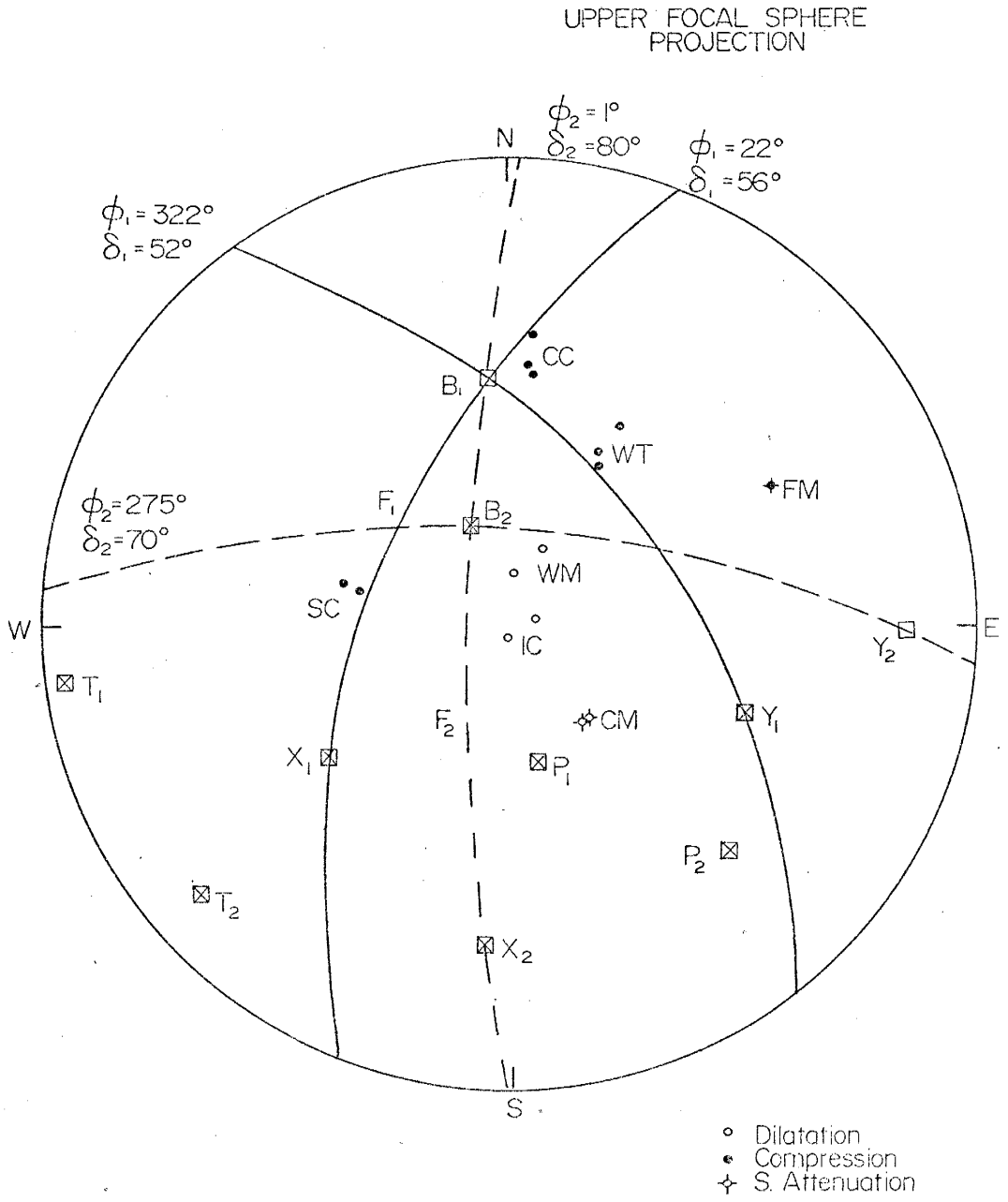

Figure 13 Composite fault-plane Solution G based on observed first motion data. The maximum clockwise (solid line) and counterclockwise (dashed line) orientations of the P nodal planes are shown.

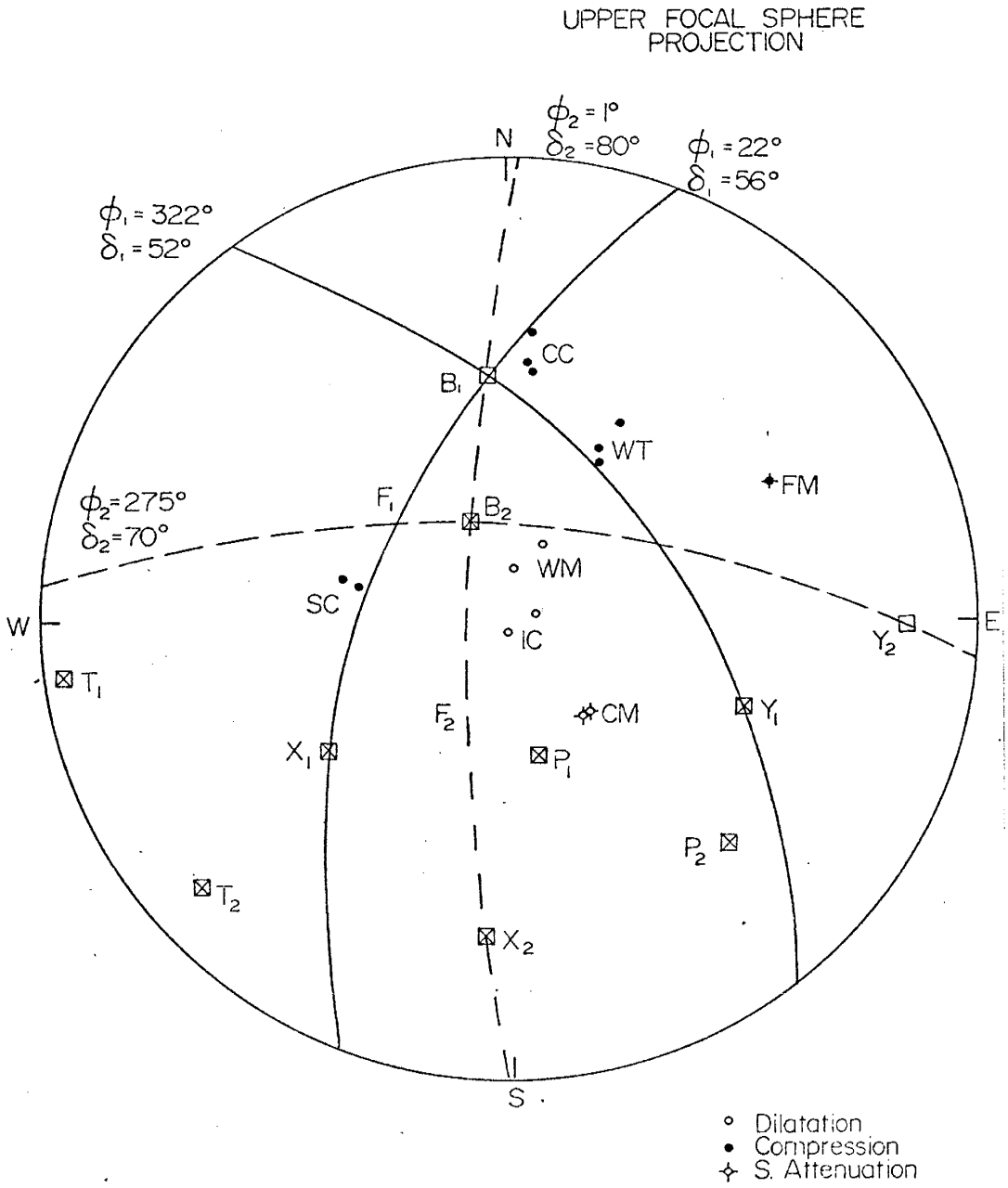

Figure 13 Composite fault-plane Solution G based on observed first motion data. The maximum clockwise (solid line) and counterclockwise (dashed line) orientations of the P nodal planes are shown.

For the remaining seven solutions (Solutions C, E, I, J, K, L, M) the number and/or azimuthal distribution of recorded first motions was inadequate to constrain the solution. In these cases, two basically different types of faulting could be interpreted from the distribution of first motions.

Solution E (Figure 14) is based on data from 16 micro-earthquakes with an average focal depth of 7.9 km located along the eastern margin of the Socorro Mountains (Figure 3(b)). Solution 1 indicates dominantly normal faulting on a plane striking N 03° E and dipping 54° W. Solution 2 indicates dominantly right-hand strike-slip faulting on a plane striking N 39° W and dipping 76° SW. As before, the P nodal planes having the greatest dip were chosen as the fault-plane.

Solution C (Figure 15) is based on data from 4 micro-earthquakes with an average focal depth of 5.7 km located beneath the western margin of the Socorro Mountains (Figure 3(c)). Solution 1 indicates dominantly normal faulting on a plane striking N 23° E and dipping 50° E. Solution 2 indicates dominantly right-hand strike-slip faulting on a plane striking N 88° W and dipping 76° N.

Solution M (Figure 16) is based on data from 2 micro-earthquakes with an average focal depth of 5.0 km located in the elevated crustal block east of the Rio Grande Valley (Figure 3(b)). Solution 1 indicates dominantly normal faulting on a plane striking N 44° W and dipping 54° NE. Solution 2 indicates dominantly left-hand strike-slip faulting on a plane striking N 02° W and dipping 90°.

Solution I (Figure 17) is based on data from 2 micro-earthquakes with an average focal depth of 8.4 km located towards the southern end of the La Jencia basin (Figure 3(b)). Solution 1 indicates dominantly normal faulting on a plane striking N 15° W and dipping 50° W. Solution 2 indicates pure right-hand strike-slip faulting on a plane striking N 66° W and dipping 90°.

Solution L (Figure 18) is based on data from 3 micro-earthquakes with an average focal depth of 6.3 km located on the western margin of the Socorro Mountains (Figure 3(b)). Solution 1 indicates pure normal faulting on a plane striking N 35° W and dipping 46° SW. Solution 2 indicates dominantly left-hand strike-slip faulting on a plane striking N 06° E and dipping 80° W.

Solution J (Figure 19) is based on data from 2 micro-earthquakes with an average focal depth of 6.1 km located in the southern La Jencia basin (Figure 3(b)). Solution 1 indicates dominantly reverse faulting on a plane striking N 14° E and dipping 50° W. It should be noted that this was the only case of reverse faulting to be found in this study. Solution 2 indicates dominantly right-hand strike-slip motion on a plane striking E - W and with a dip of 74° N.

Solution K (Figure 20) is based on data from 2 micro-earthquakes with an average focal depth of 4.9 km located on the eastern margin of the Chupadera Mountains (Figure 3(b)). Solution 1 indicates pure normal faulting on a plane striking N 07° W and dipping 55° E. Solution 2 indicates dominantly right-hand strike-slip faulting on a plane striking N 61° W

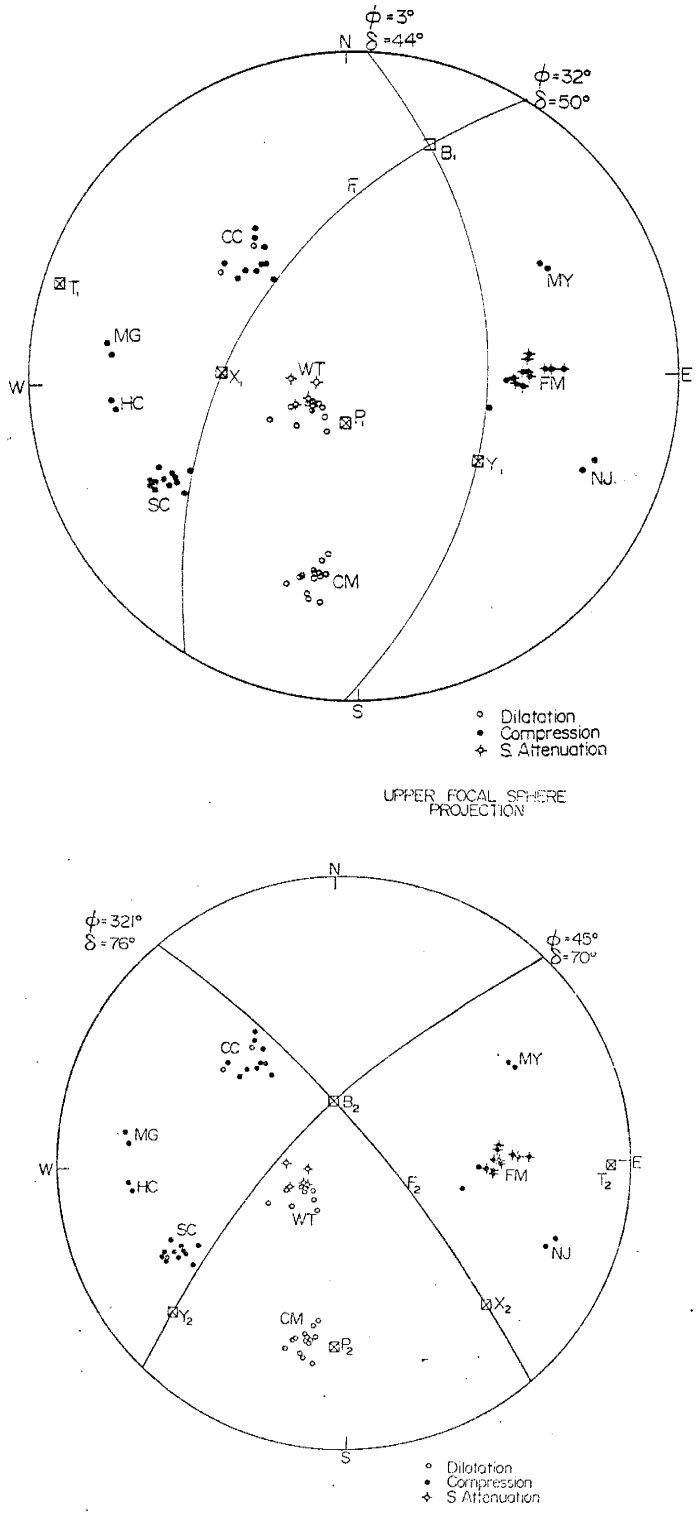

Figure 14 Composite fault-plane Solution E based on observed first motion data. The two basically different interpretations are shown.

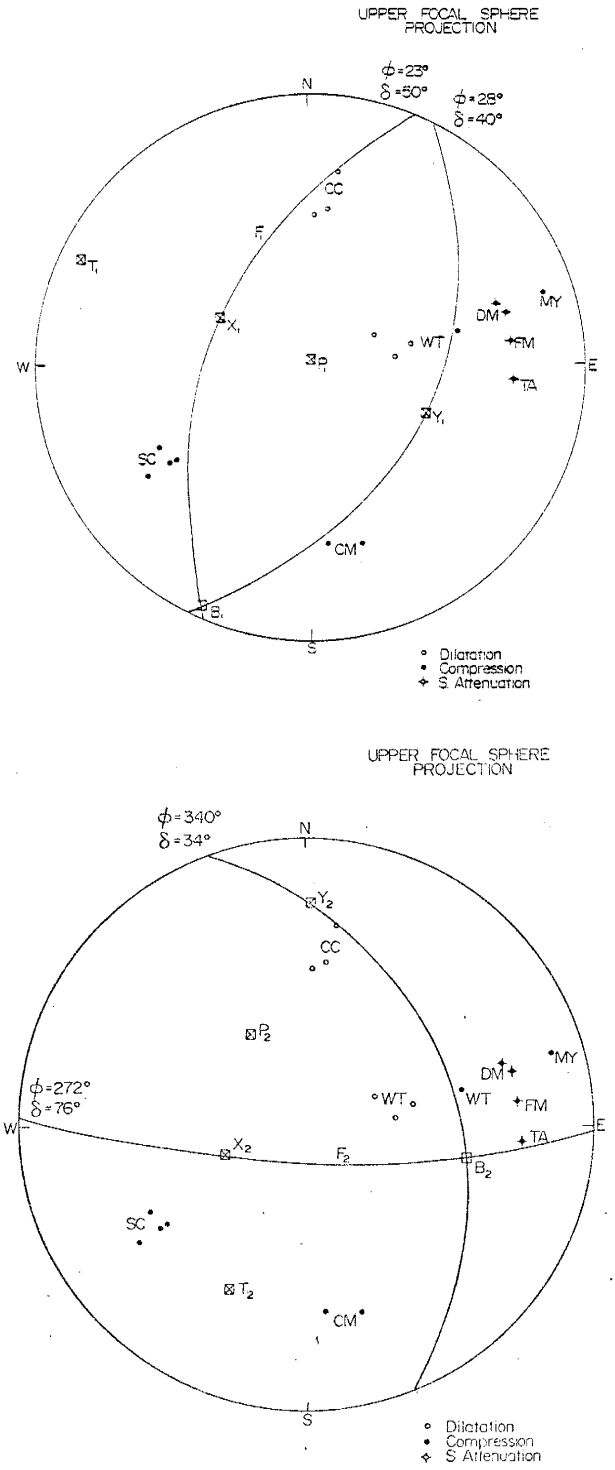

Figure 15 Composite fault-plane Solution C based on observed first motion data. The two basically different interpretations are shown.

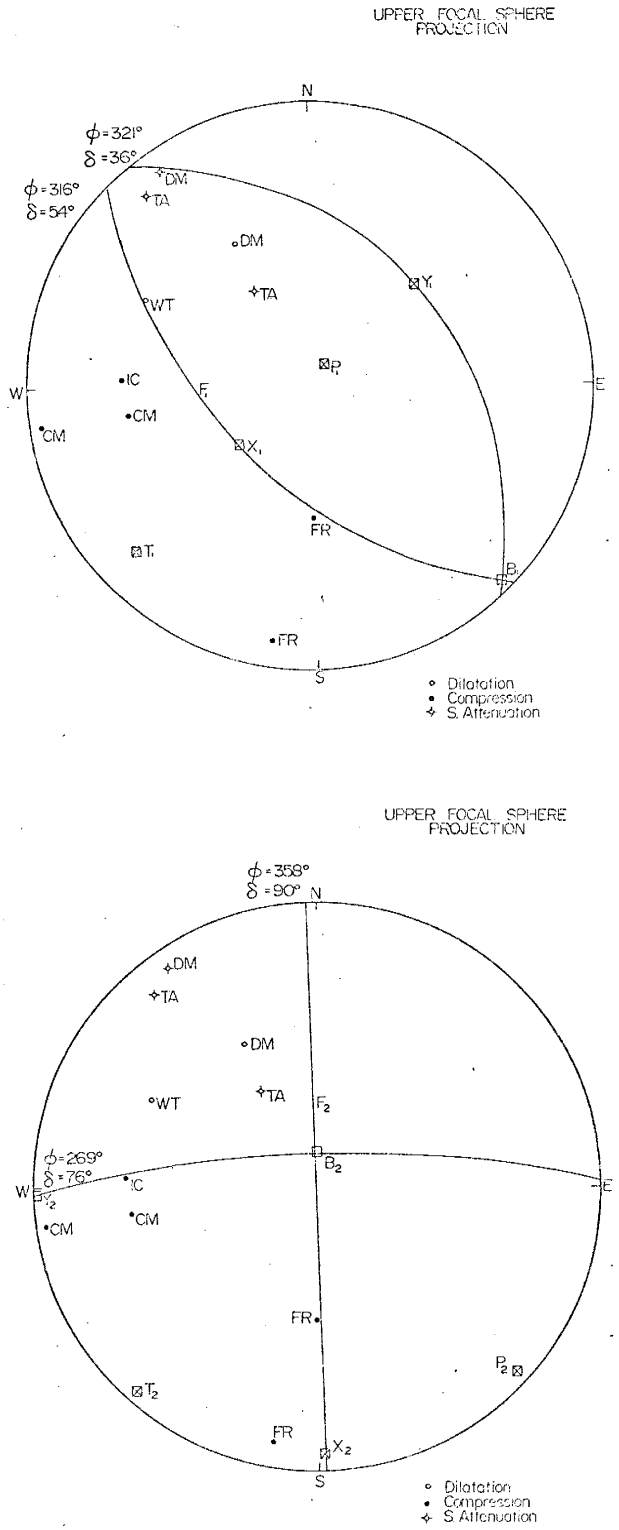

Figure 16 Composite fault-plane Solution M based on observed first motion data. The two basically different interpretations are shown.

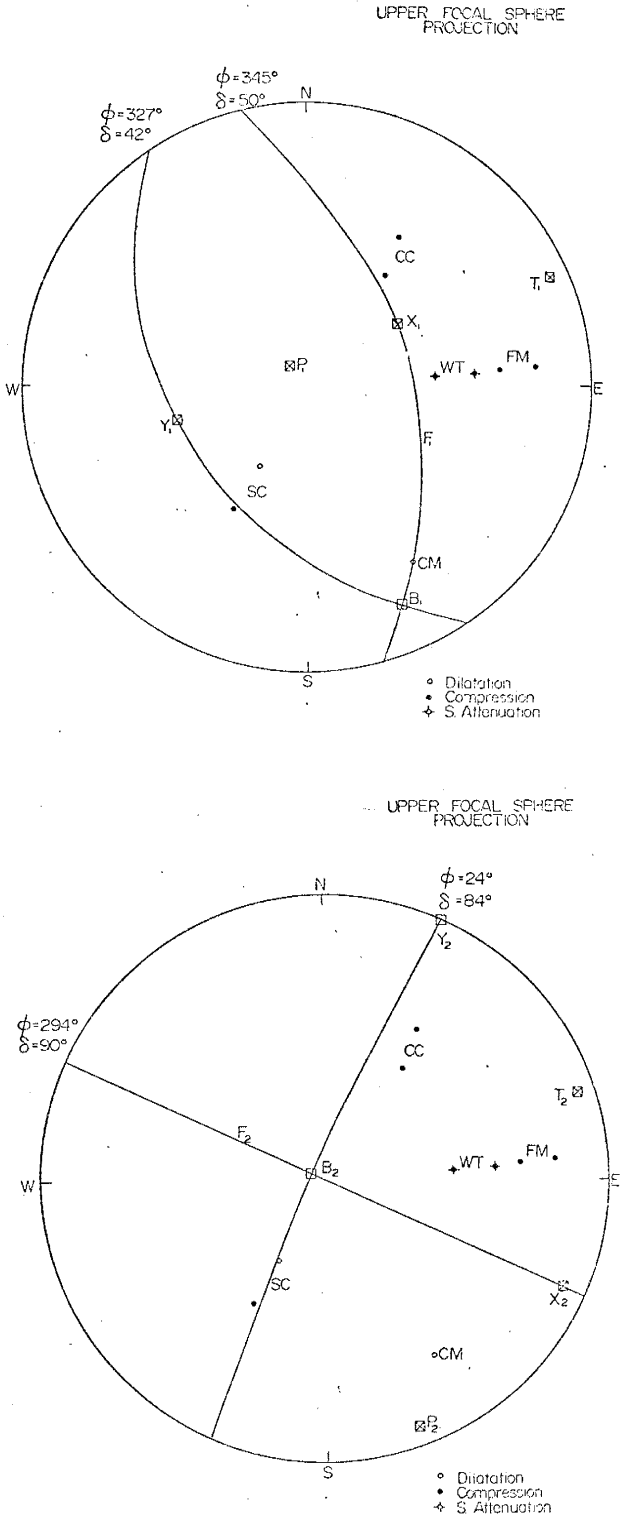

Figure 17 Composite fault-plane Solution I based on observed first motion data. The two basically different interpretations are shown.

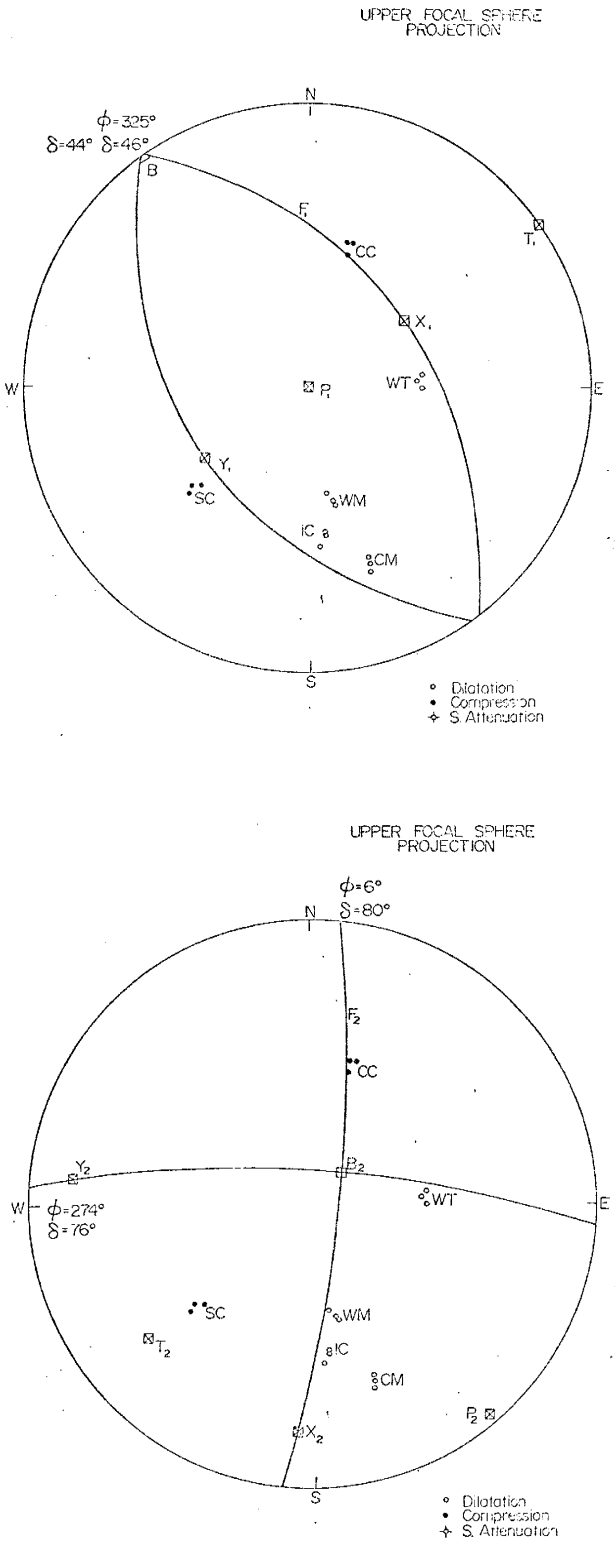

Figure 18 Composite fault-plane Solution L based on observed first motion data. The two basically different interpretations are shown.

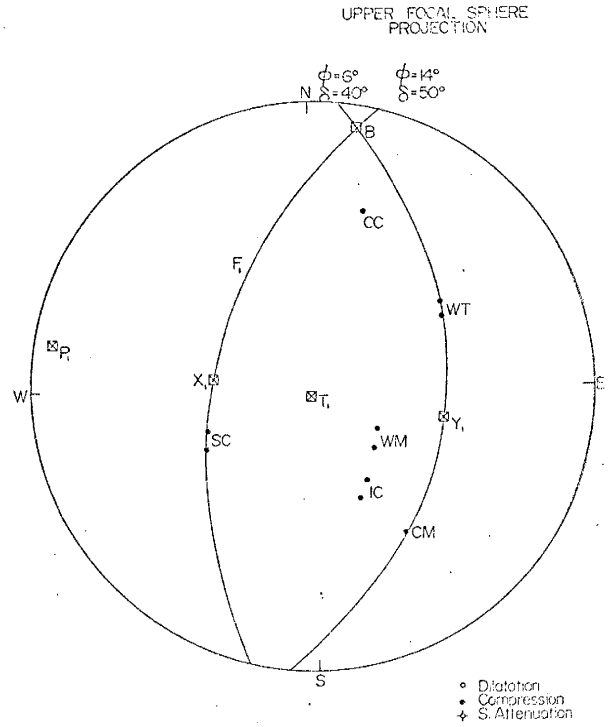

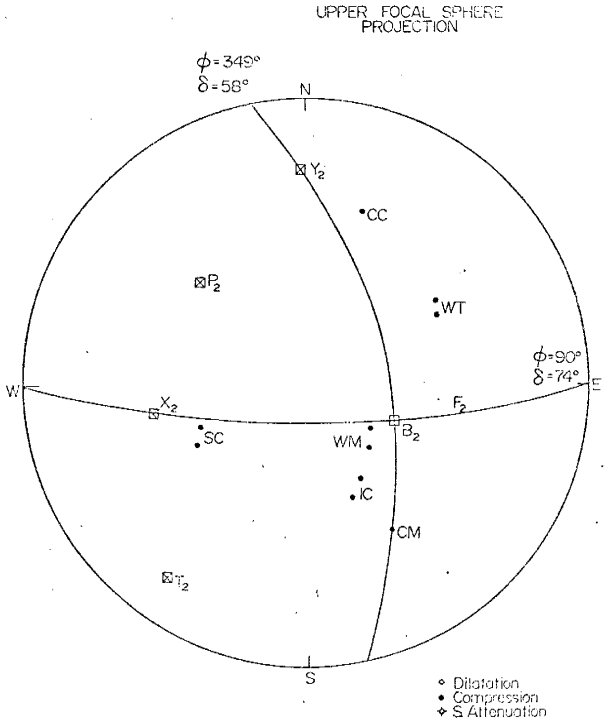

Figure 19 Composite fault-plane Solution J based on observed first motion data. The two basically different interpretations are shown.

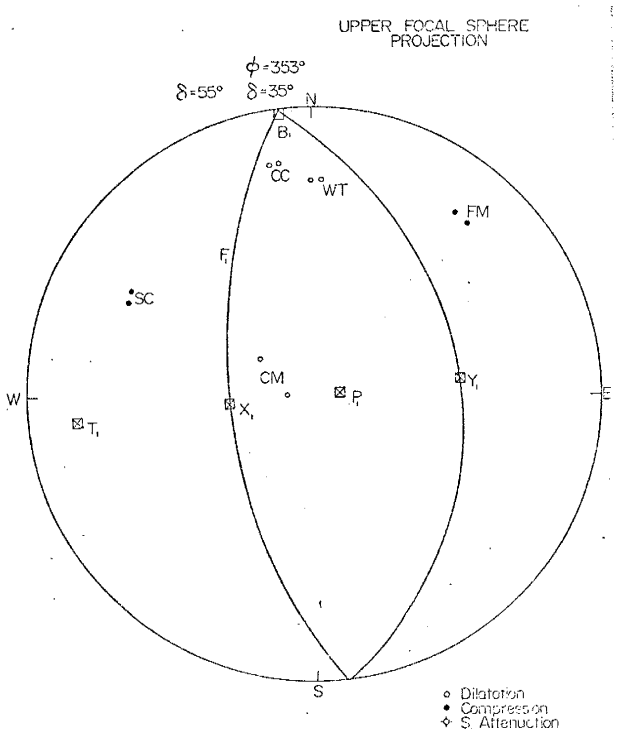

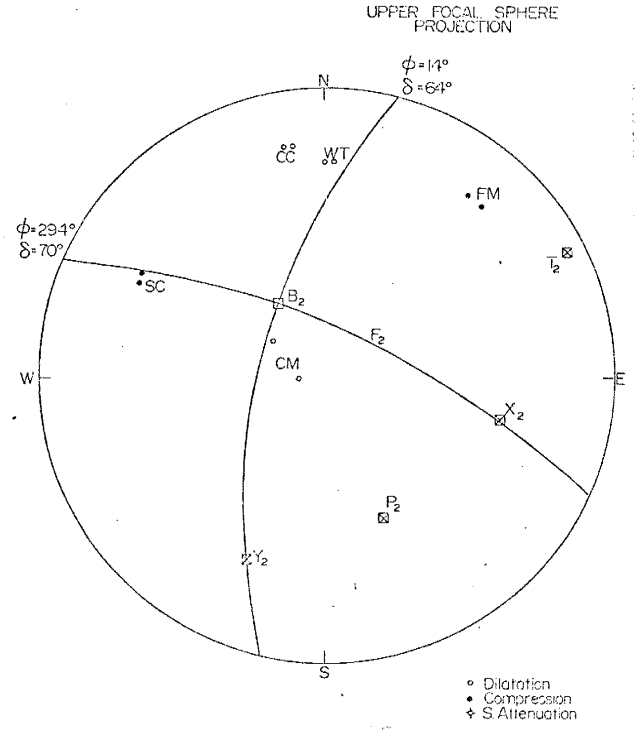

Figure 20 Composite fault-plane Solution K based on observed first motion data. The two basically different interpretations are shown.

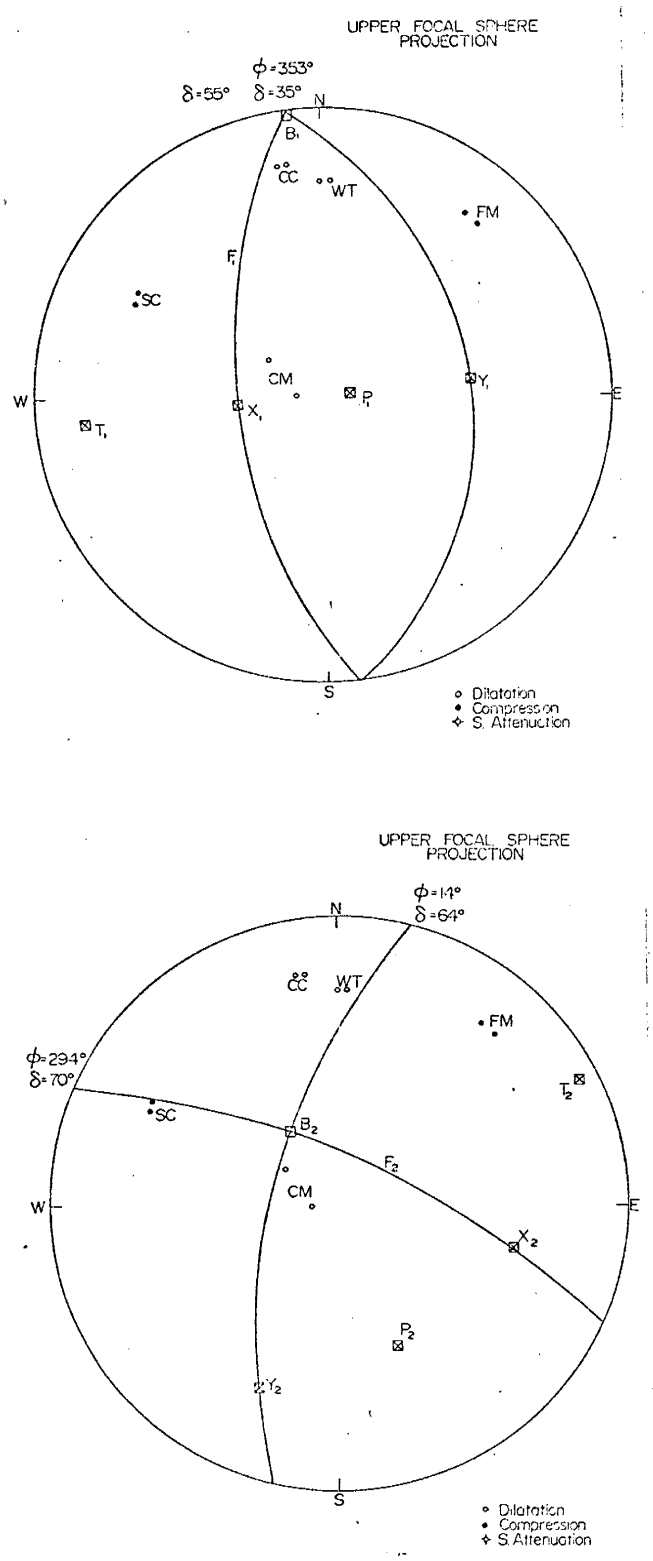

Figure 20 Composite fault-plane Solution K based on observed first motion data. The two basically different interpretations are shown.

and dipping 70° SW.

Preferred Focal Plane Solutions Using Amplitudes of SV Phases

An additional means of constraining the focal plane solutions was to make the observed SV amplitudes compatible with the computed SV nodal planes.

In this study, the ratio of the recorded P wave amplitude to the SV wave amplitude, W_p/W_{sv}, was used as a measure of the strength of the S phase. The use of this ratio eliminated the need to correct for the effects of geometrical spreading and attenuation of the seismic waves along their travel paths. The ratio was determined by reading the maximum peak to peak amplitude (MM) of both the P and SV waves within the first 5 cycles of each phase as recorded on the seismogram. Values of $W_p/W_{sv} \geq 1.50$ were arbitrarily specified as showing "S wave attenuation" (the near or total lack of S wave motion). Observational points on the stereographic projection that had these large W_p/W_{sv} values are shown as crossed circles.

Theoretical SV nodal planes were constructed using the expression for the SV displacement given by Herrmann (1975); the resulting SV nodal plane being a third order conical surface. In general, preferred composite solutions were then constructed using the first motion and amplitude data such that (a) the resulting solutions were compatible with the first motion data and (b) the resulting orientations of the SV nodal planes were compatible with the amplitude data. In the latter case, the SV nodal planes were not allowed to

pass through any observational points on the stereonet having high SV wave amplitudes, but only through observational points having low SV wave amplitudes or through areas where no first motion and amplitude data were available. In the preferred solutions shown in Figures 21 through 29, the fault-plane was chosen as the P nodal plane having the greatest dip.

The interpretation of low SV wave amplitudes as an indication of a SV nodal plane may not necessarily be true. Low SV wave amplitudes may also result when S waves pass through molten or partially molten rock (magma bodies). A further discussion of this possibility will be given in a later section.

Nine preferred composite solutions (Solutions A, H, N, D, F, B, G, E, I) were constructed following the general procedure outlined above. Each of the nine solutions will be discussed separately as to what specific constraints were used in the interpretation.

Solution A (Figure 21) indicates dominantly normal faulting on a plane striking N 24° E and dipping 68° E. The factors considered in selecting this preferred solution in addition to the distribution of first motions were the low amplitude SV signals at stations IC and WM.

Solution H (Figure 22) indicates dominantly normal faulting on a plane striking N 10° W and dipping 54° E. The factor considered in selecting this preferred solution in addition to the distribution of first motions was the low amplitude SV signals at station WT.

Solution N (Figure 23) indicates dominantly normal faulting on a plane striking N 12° W and dipping 54° E. The factor considered in selecting this preferred solution in addition to the distribution of first motions was the low amplitude SV signal at station SC.

Solution D (Figure 24) indicates dominantly normal faulting on a plane striking N 18° W and dipping 64° E. The factor considered in selecting this preferred solution in addition to the distribution of first motions was the low amplitude SV signals at station WT.

Solution F (Figure 25) indicates dominantly normal faulting on a plane striking N 48° W and dipping 52° SW. The factors considered in selecting this preferred solution in addition to the distribution of first motions were the high amplitude SV signals at stations CC and CM.

Solution B (Figure 26) indicates dominantly normal faulting on a plane striking N 20° W and dipping 64° W. The factors considered in selecting this preferred solution in addition to the distribution of first motions were the low amplitude SV signals at stations SC, FM and TA.

Solution G (Figure 27) indicates a combination of normal faulting and right-hand strike-slip faulting on a plane striking N 06° W and dipping 56° E. The factors considered in selecting this preferred solution in addition to the distribution of first motions were the high amplitude SV signals at station CC and the low amplitude SV signals at station CM. Reasonably high W_p/W_{sv} amplitude ratios (low SV amplitude) of 0.97 and 0.93 at station IC were also considered.

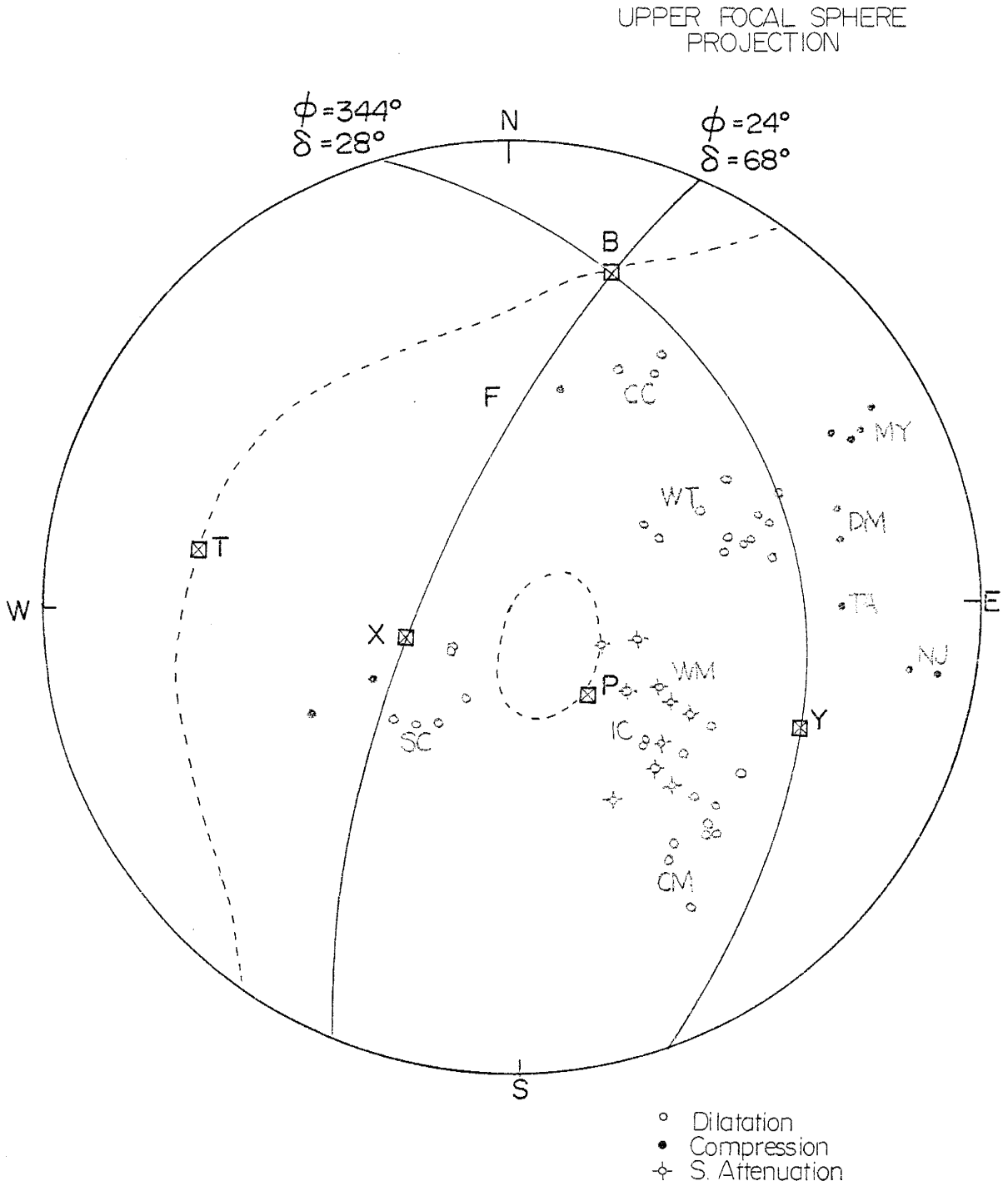

Figure 21. Preferred composite fault-plane solution A based on first motion and SV amplitude data. The P nodal planes are shown by the solid lines; the SV nodal planes by the dashed lines.

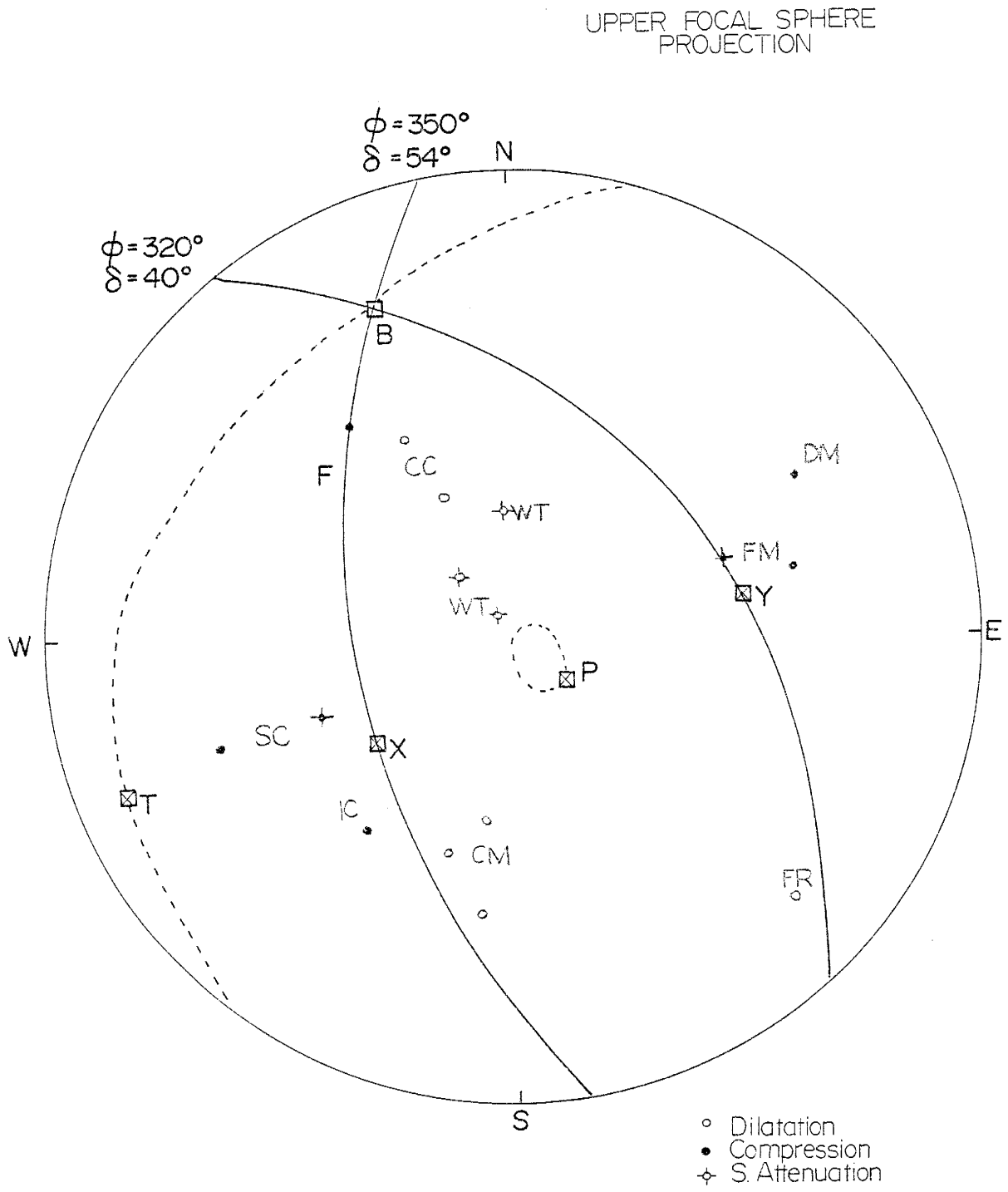

Figure 22 Preferred composite fault-plane solution H based on first motion and SV amplitude data. The P nodal planes are shown by the solid lines; the SV nodal planes by the dashed lines.

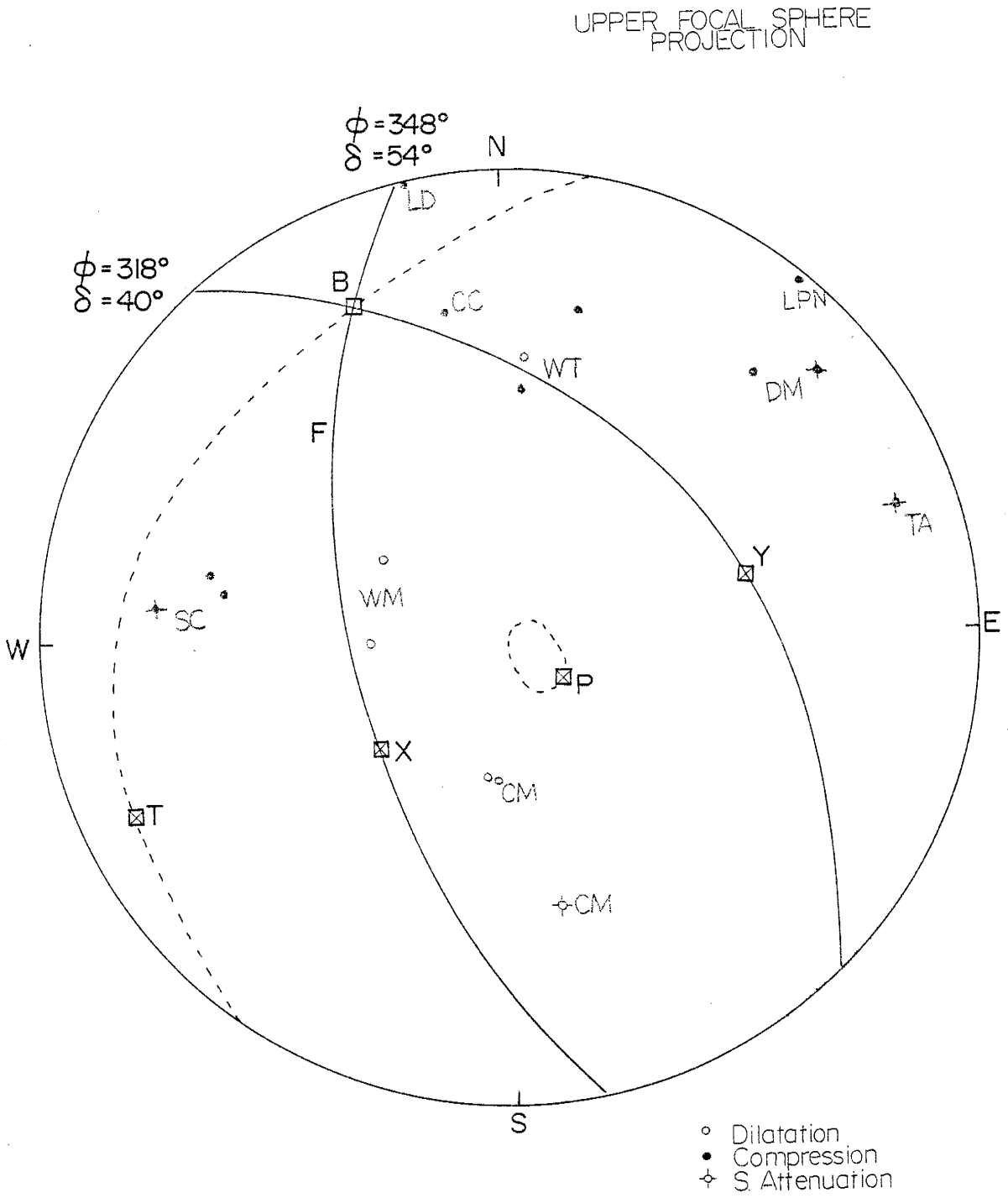

Figure 23 Preferred composite fault-plane Solution N based on first motion and SV amplitude data. The P nodal planes are shown by the solid lines; the SV nodal planes by the dashed lines.

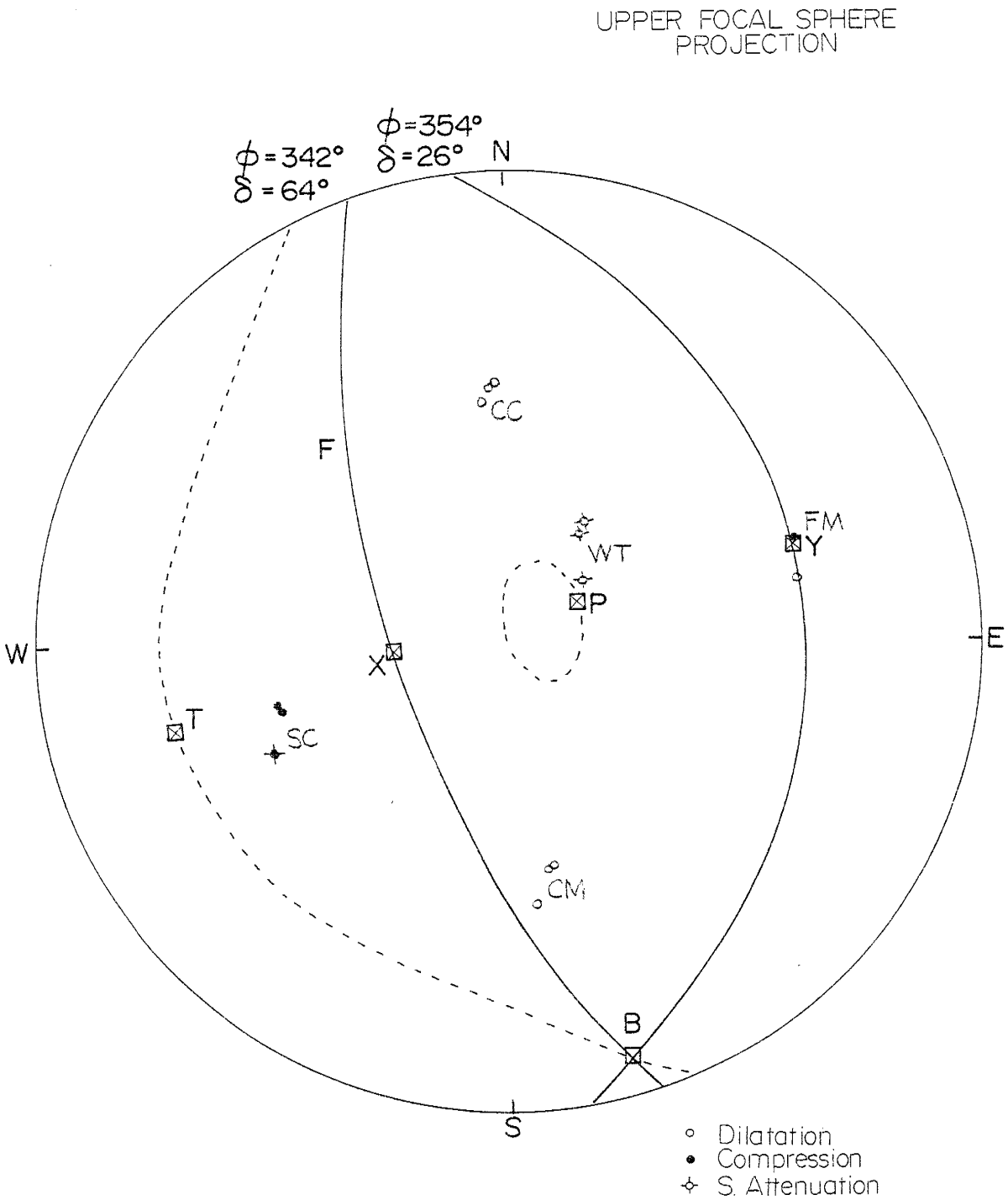

Figure 24 Preferred composite fault-plane Solution D based on first motion and SV amplitude data. The P nodal planes are shown by the solid lines; the SV nodal planes by the dashed lines.

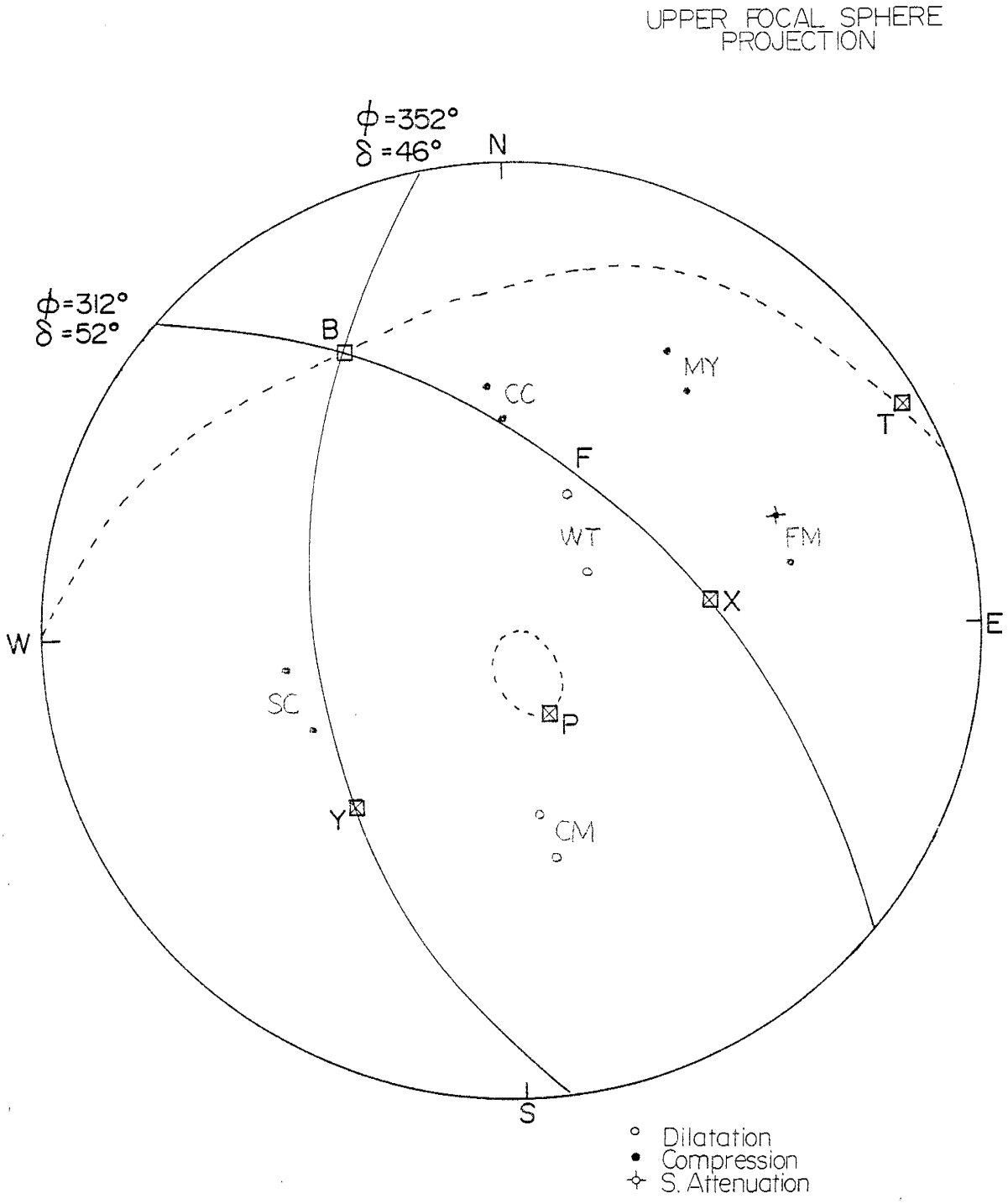

Figure 25 Preferred composite fault-plane Solution F based on first motion and SV amplitude data. The P nodal planes are shown by the solid lines; the SV nodal planes by the dashed lines.

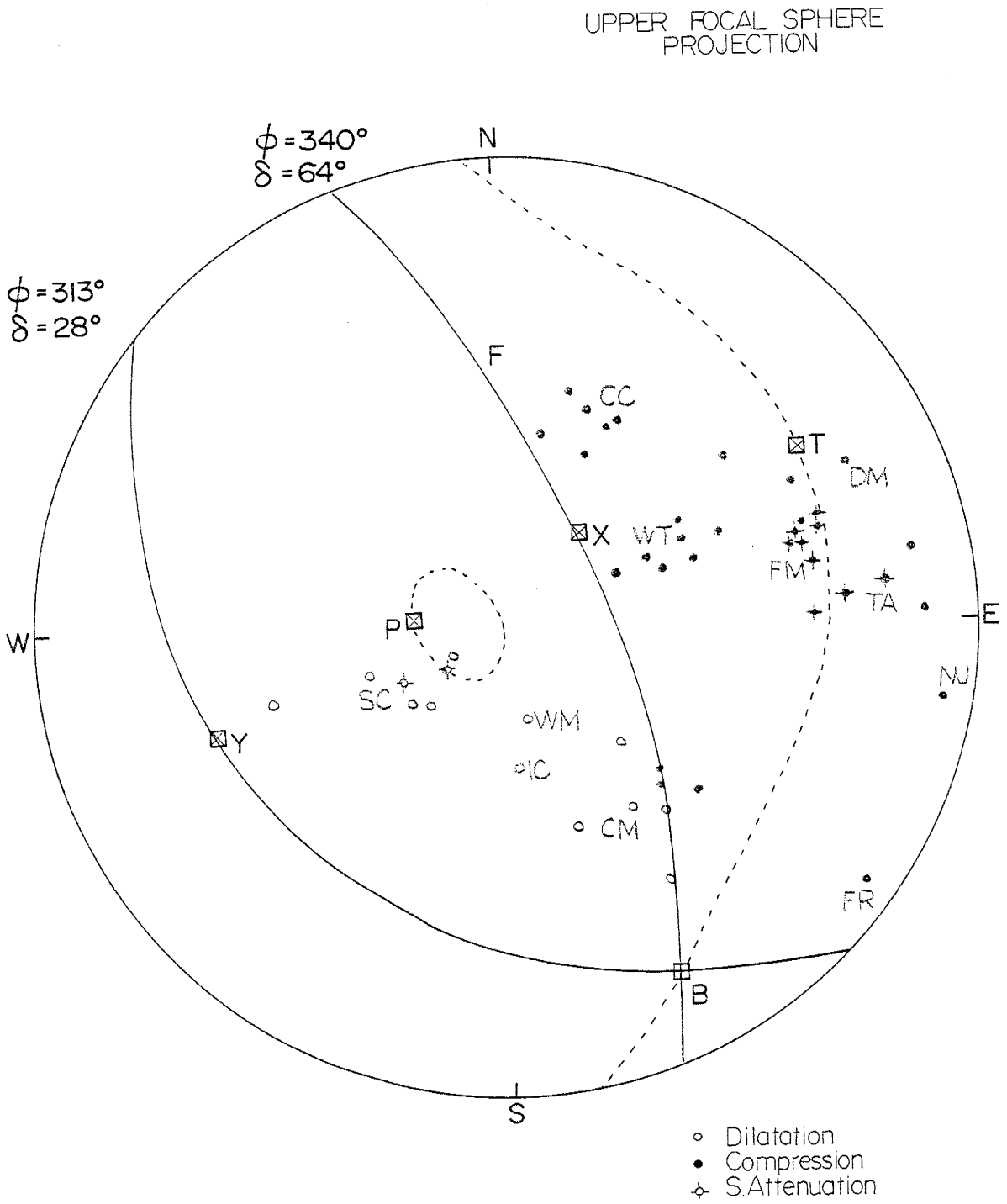

Figure 26 Preferred composite fault-plane Solution 3 based on first motion and SV amplitude data. The P nodal planes are shown by the solid lines; the SV nodal planes by the dashed lines.

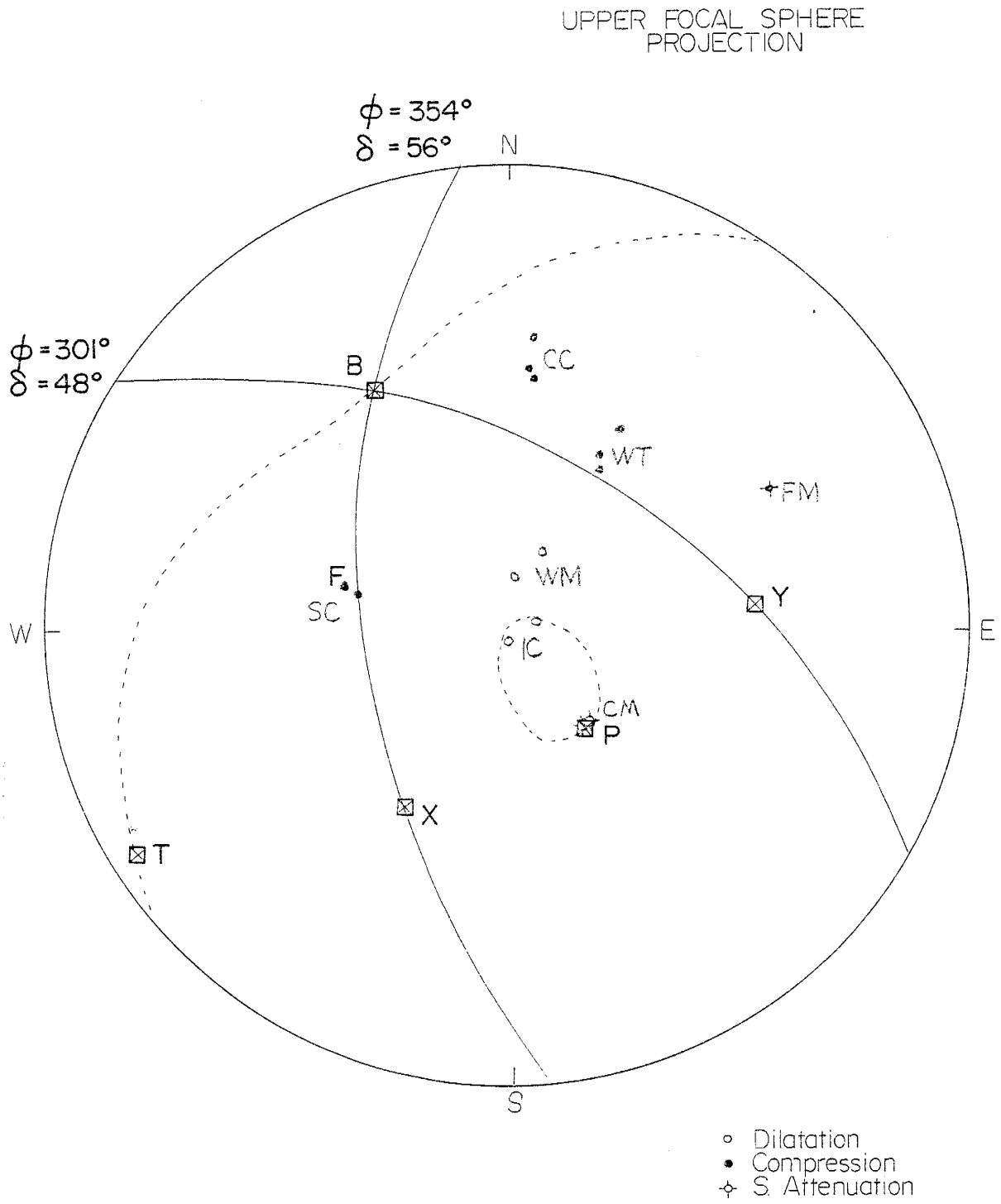

Figure 27 Preferred composite fault-plane solution G based on first motion and SV amplitude data. The P nodal planes are shown by the solid lines; the SV nodal planes by the dashed lines.

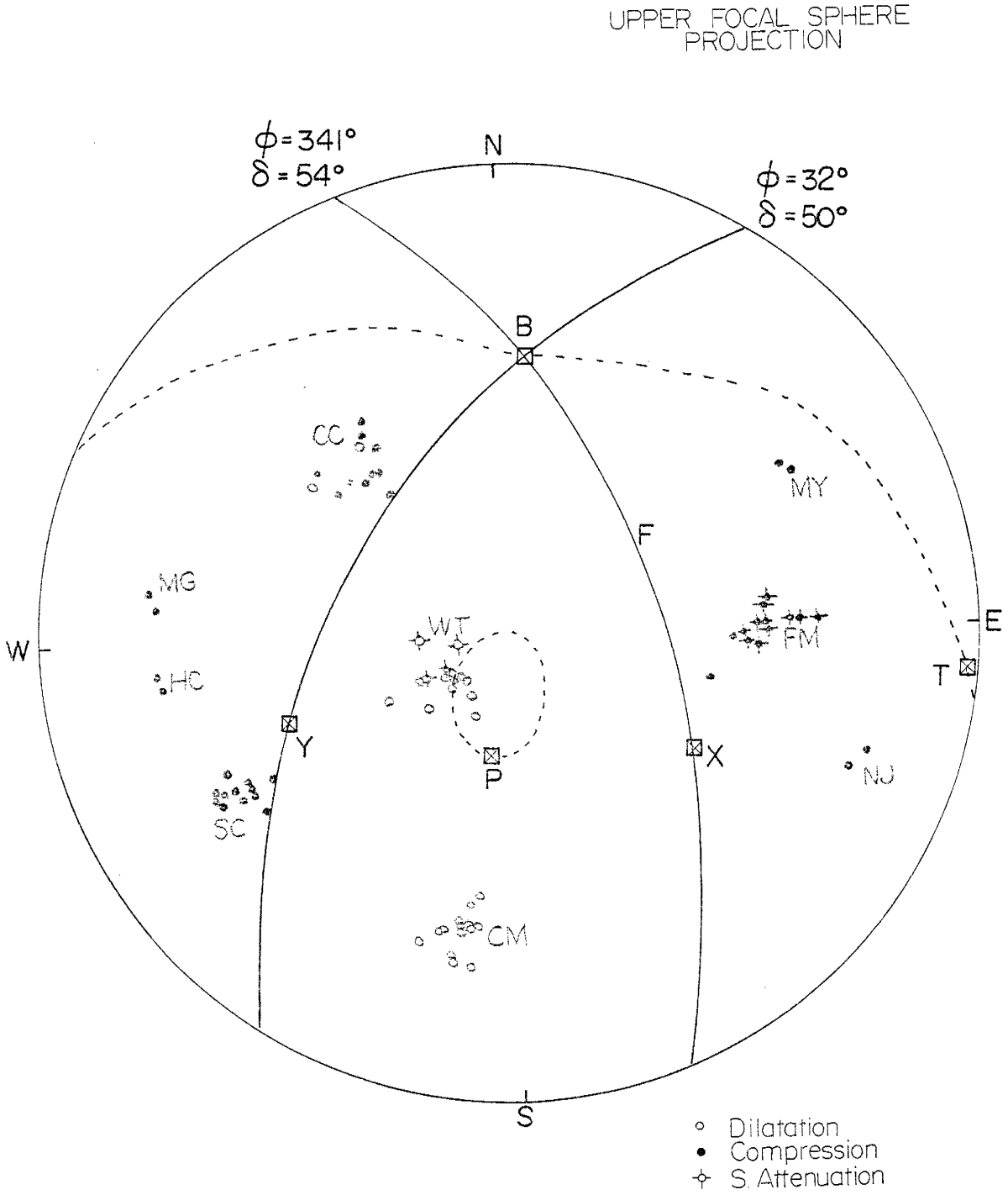

Figure 26 Preferred composite fault-plane solution 3 based on first motion and SV amplitude data. The P nodal planes are shown by the solid lines; the SV nodal planes by the dashed lines.

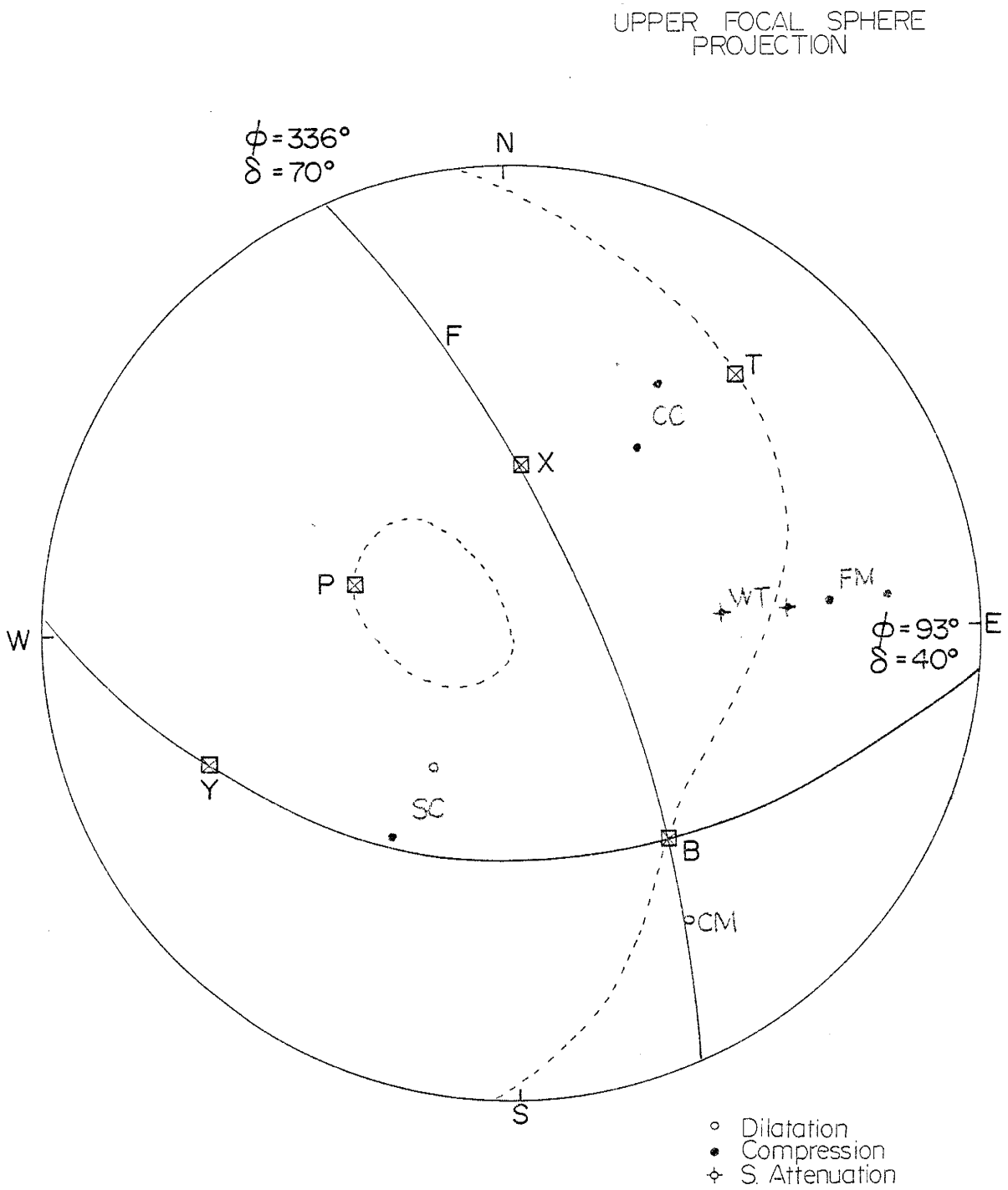

Figure 29 Preferred composite fault-plane Solution I based on first motion and SV amplitude data. The P nodal planes are shown by the solid lines; the SV nodal planes by the dashed lines.

Solution II (Figure 28) indicates a combination of normal faulting and right-hand strike-slip faulting on a plane striking N 19° W and dipping 54° W. The factor considered in selecting this preferred solution in addition to the distribution of first motions was the low amplitude SV signals at station WT.

Solution I (Figure 29) indicates a combination of normal faulting and left-hand strike-slip motion on a plane striking N 24° W and dipping 70° W. The factor considered in selecting this preferred solution in addition to the distribution of first motions was the low amplitude SV signals at station WT.

The azimuth and plunge for the preferred principal axes are listed in Table 3. Observation data for each solution are given in Table 4.

Table 3

Azimuth and Plunge of Principal Axes for Focal Plane Solutions

Solution		Range of Values										Preferred Values				
		P_1	T_1	B_1	X_1	Y_1	P_2	T_2	B_2	X_2	Y_2	P	T	B	X	Y
A	AZ	125	302	23	295	115	142	280	18	253	113	142	280	18	253	113
	Plunge	68	22	03	66	24	62	22	16	62	22	62	22	16	62	22
H	AZ	132	247	339	231	80	142	233	324	206	80	132	247	339	231	80
	Plunge	74	06	15	50	36	59	01	31	38	36	74	06	15	50	36
N	AZ	127	245	337	228	78	102	228	332	205	63	127	245	337	228	78
	Plunge	73	07	15	50	36	68	12	17	55	30	73	07	15	50	36
D	AZ	119	276	09	274	102	98	233	328	211	67	60	256	164	264	71
	Plunge	68	18	07	63	24	64	18	17	56	28	71	19	05	64	26
F	AZ	140	255	349	222	105	116	214	304	202	45	160	61	330	82	222
	Plunge	52	04	37	38	30	78	00	12	44	46	69	03	21	44	38
B	AZ	200	111	06	138	250	276	61	155	43	250	276	61	155	43	250
	Plunge	48	06	41	38	26	68	18	12	61	26	68	18	12	61	26
G	AZ	169	263	355	234	111	136	230	337	185	91	142	239	332	211	84
	Plunge	56	02	34	38	34	23	07	67	21	10	60	04	29	42	34
E	AZ	188	289	20	273	122	183	91	254	136	242	190	96	05	122	250
	Plunge	74	03	15	46	40	24	04	64	20	12	61	02	29	40	36
C	AZ	26	295	205	297	113	329	206	100	251	02					
	Plunge	88	05	02	50	40	49	26	30	56	14					
M	AZ	35	228	137	231	46	134	222	358	181	269					
	Plunge	80	10	03	54	36	03	03	76	04	01					

Table 3 Continued

Solution		Range of Values										Preferred Values				
		P_1	T_1	B_1	X_1	Y_1	P_2	T_2	B_2	X_2	Y_2	P	T	B	X	Y
I	AZ	314	66	157	56	255	160	71	115	24	335	287	43	144	04	248
	Plunge	80	05	10	48	40	04	05	06	00	84	53	19	33	52	20
L	AZ	242	55	325	54	232	140	225	35	185	276					
	Plunge	89	01	00	46	44	02	18	72	14	10					
J	AZ	280	190	11	275	104	304	217	113	259	00					
	Plunge	04	86	04	50	40	37	11	53	32	16					
K	AZ	86	264	353	264	86	158	63	328	103	204					
	Plunge	80	10	00	65	35	34	04	56	26	20					
COMPOSITE SOLUTION*																
	AZ											148	260	350	248	90
	Plunge											78	04	12	48	40

* - Composite of Solutions A, B, C, D, E, F, G, H, I, K, L, M, N

Table 4

Fault-Plane Solution Parameters

Solution	Event Number	Station	First Motion	W_p/W_{s_v}	Azimuth (degrees)	Angle of Incidence (degrees)
A	34	WT	D	0.38	58	55
		MY	C	0.67	72	74
		CC	D	0.24	15	66
		SC	C	1.10	246	52
		CM	D	1.25	150	62
	36	WT	D	0.37	68	57
		SC	D	0.23	230	38
		CM	D	0.79	141	63
		MY	C	1.36	63	78
	40	WT	D	0.31	57	34
		CC	C	0.31	12	50
		SC	C	0.95	246	38
		CM	D	1.50	155	48
	43	WT	D	0.33	66	62
		NJ	C	0.83	99	83
		CC	D	0.65	18	70
		CM	D	0.39	151	71
		MY	C	0.94	61	81
	46	WT	D	0.28	71	50
		CC	D	0.52	23	58
		CM	D	0.90	148	61
		MY	C	0.83	63	76
		NJ	C	0.70	100	89

Table 4 Continued

Solution	Event Number	Station	First Motion	W_p/W_{s_v}	Azimuth (degrees)	Angle of Incidence (degrees)
	1A	WT	D	0.15	74	48
		SC	D	0.33	213	24
		CM	D	0.35	137	55
		WM	D	3.10	120	36
		IC	D	1.46	137	41
	3A	WT	D	0.08	63	37
		SC	D	0.09	141	18
		CM	D	0.69	138	42
		WM	D	3.15	113	21
		IC	D	2.43	139	26
	5A	WT	D	0.39	71	58
		CC	D	0.22	30	64
		SC	D	0.14	223	36
		CM	D	1.02	140	64
		WM	D	6.86	121	45
		IC	D	3.03	140	51
	6A	WT	D	0.11	61	47
		CC	D	0.14	19	60
		SC	D	0.12	245	19
		CM	D	0.95	133	49
		WM	D	3.18	103	28
		IC	D	2.52	128	32
	19A	WT	D	0.07	81	57
		CM	D	0.70	126	60

Table 4 Continued

Solution	Event Number	Station	First Motion	W_p/W_{s_v}	Azimuth (degrees)	Angle of Incidence (degrees)
		IC	D	1.45	121	51
		DM	C	0.49	77	70
		TA	C	0.77	90	71
	22A	WT	D	0.10	73	52
		CM	D	0.77	136	58
		IC	D	2.10	134	44
		DM	C	0.21	73	70
	24A	WT	D	0.19	73	54
		CC	D	0.26	31	59
		SC	D	0.12	220	32
		CM	D	0.17	140	61
		WM	D	1.82	123	41
		IC	D	2.63	140	47
B	6	WT	C	0.68	60	46
		FM	C	7.50	74	67
		CC	C	0.75	18	56
		SC	D	1.57	248	34
		CM	D	0.19	145	51
	12	WT	C	0.43	64	37
		FM	C	3.50	74	57
		CC	C	0.75	26	44
		SC	D	1.00	141	14
		CM	D	0.65	134	38
	19	FM	C	8.00	75	64

Table 4 Continued

Solution	Event Number	Station	First Motion	W_p/W_{s_v}	Azimuth (degrees)	Angle of Incidence (degrees)
		CC	C	0.52	28	52
		SC	D	6.56	235	16
		CM	C	0.08	133	47
	38	WT	C	0.57	70	46
		FM	C	8.57	78	67
		CC	C	0.60	29	53
		SC	D	1.04	225	25
		CM	D	0.14	139	53
	48	WT	C	1.35	64	45
		FM	C	5.00	75	66
		CC	C	0.63	23	54
		SC	D	1.85	143	27
	9A	WT	C	0.31	70	39
		SC	D	1.05	231	29
		CM	D	0.28	146	50
		DM	C	1.01	71	70
		TA	C	3.83	89	66
	10A	WT	C	0.34	54	60
		SC	D	0.41	253	44
		CM	C	0.89	137	60
		DM	C	1.35	65	77
		TA	C	1.76	34	78
	18A	WT	C	0.35	67	28
		CM	D	0.68	159	48

Table 4 Continued

Solution	Event Number	Station	First Motion	W_p/W_{s_v}	Azimuth (degrees)	Angle of Incidence (degrees)
		CC	C	0.29	12	44
		IC	D	2.11	174	33
		WM	D	0.73	166	22
	33A	WT	C	0.54	64	68
		CM	C	0.21	155	77
		DM	C	1.45	70	82
		TA	C	1.13	89	83
		NJ	C	1.25	100	85
		FR	C	0.58	126	85
	34A	WT	C	0.25	68	52
		CM	C	0.03	132	55
		DM	C	0.81	71	70
		TA	C	5.41	86	71
C	41	WT	C	0.30	77	58
		CC	D	0.14	09	71
		SC	C	1.36	235	71
		MY	C	0.69	63	83
	51	WT	D	0.39	79	41
		FM	C	6.50	83	73
		CC	D	0.33	07	59
		SC	C	0.28	235	62
		CM	C	0.20	164	69
	8A	WT	D	0.76	66	26
		SC	C	0.28	241	64

Table 4 Continued

Solution	Event Number	Station	First Motion	W_p/W_{s_v}	Azimuth (degrees)	Angle of Incidence (degrees)
		CM	C	0.44	174	66
		DM	C	3.52	72	71
		TA	C	6.48	94	73
	16A	WT	D	0.52	84	36
		CC	D	0.09	03	58
		SC	C	0.48	235	64
		DM	C	2.61	75	73
D	14	WT	D	2.50	34	34
		FM	C	0.40	71	66
		CC	D	0.28	358	58
		SC	C	1.01	258	53
		CM	D	0.73	169	51
	16	WT	D	2.25	36	31
		FM	C	0.25	72	65
		CC	D	0.38	357	56
		SC	C	1.10	253	53
		CM	D	0.42	70	51
	30	WT	D	1.86	52	23
		FM	D	0.15	79	65
		CC	D	0.17	355	53
		SC	C	1.81	245	57
		CM	D	0.08	173	58
E	5	CM	D	0.43	199	67

Table 4 Continued

Solution	Event Number	Station	First Motion	W_p/W_{s_v}	Azimuth (degrees)	Angle of Incidence (degrees)
		WT	D	5.42	244	33
		FM	C	3.33	93	52
		CC	C	0.56	310	55
		SC	C	0.24	244	70
	10	WT	D	6.87	247	22
		FM	C	2.67	89	61
		CC	C	0.20	322	56
		SC	C	0.27	243	69
		CM	D	0.40	193	68
	15	WT	D	2.02	246	17
		FM	C	1.90	89	55
		CC	C	0.22	323	49
		CM	D	0.46	192	63
		MY	C	1.22	60	68
	21	WT	D	1.90	315	15
		FM	C	2.88	68	66
		SC	C	0.03	242	70
		CM	D	0.36	189	70
		CC	C	0.15	328	58
	23	WT	D	0.97	228	13
		FM	C	1.01	91	51
		SC	C	0.51	240	60
		CM	D	0.96	190	59
	25	WT	D	1.20	234	16

Table 4 Continued

Solution	Event Number	Station	First Motion	W_p/W_{s_v}	Azimuth (degrees)	Angle of Incidence (degrees)
		FM	C	2.83	90	57
		CC	C	0.13	324	48
		CM	D	0.50	191	64
		MY	C	0.60	61	68
	26	WT	D	1.18	246	24
		FM	C	6.00	91	52
		CC	C	0.23	316	50
		SC	C	0.33	243	66
		CM	D	0.93	196	64
	28	WT	D	1.12	232	18
		FM	C	2.50	91	58
		CC	C	0.43	322	50
		SC	C	0.21	241	66
		CM	D	0.80	195	65
	29	WT	D	1.05	217	17
		FM	C	3.12	94	55
		CC	C	0.22	321	43
		CM	D	0.54	189	63
	32	WT	D	1.80	272	22
		FM	C	2.37	83	57
		CC	C	0.46	324	56
		SC	C	0.18	247	67
		CM	D	0.76	196	64
	35	WT	D	2.65	264	13

Table 4 Continued

Solution	Event Number	Station	First Motion	W_p/W_{S_V}	Azimuth (degrees)	Angle of Incidence (degrees)
		FM	C	3.34	85	57
		CC	C	0.34	327	52
		SC	C	0.22	245	65
		CM	D	0.92	192	63
	37	FM	C	3.18	88	63
		CC	C	0.50	324	58
		SC	C	0.36	243	70
		CM	D	0.12	192	69
	44	WT	D	1.13	230	25
		MG	C	0.99	277	74
		HC	C	1.20	264	73
		NJ	C	0.53	113	74
	45	WT	D	1.04	236	15
		CM	D	0.93	191	63
		NJ	C	0.67	110	76
		MG	C	1.12	280	75
		HC	C	1.30	266	74
	52	WT	D	1.81	238	16
		FM	C	2.58	90	56
		CC	C	0.58	323	47
		SC	C	0.18	241	64
		CM	D	0.84	191	63
	55	WT	D	1.44	205	21
		FM	C	1.26	103	46

Table 4 Continued

Solution	Event Number	Station	First Motion	W_P/W_{S_V}	Azimuth (degrees)	Angle of Incidence (degrees)
		CM	D	0.82	189	58
		SC	C	0.09	234	58
F	11	WT	D	0.59	52	23
		FM	C	0.91	78	62
		CC	C	0.18	358	49
		SC	C	1.12	246	50
		CM	D	0.68	170	52
		MY	C	0.99	30	68
	27	WT	D	0.22	22	35
		FM	C	1.67	67	62
		CC	C	0.10	355	55
		SC	C	0.78	262	52
		CM	D	0.50	172	41
		MY	C	1.00	38	64
G	22	WT	C	0.17	29	43
		FM	C	1.57	68	64
		CC	C	1.13	06	57
		SC	C	0.23	283	36
		CM	D	1.70	140	29
	26A	WT	C	0.42	30	52
		CC	C	0.29	07	63
		IC	D	0.97	73	06
		WM	D	0.46	22	20

Table 4 Continued

Solution	Event Number	Station	First Motion	W_p/W_{s_v}	Azimuth (degrees)	Angle of Incidence (degrees)
	29A	WT	C	0.23	27	45
		CC	C	0.25	04	59
		SC	C	0.65	284	40
		CM	D	2.10	209	29
		IC	D	0.93	197	03
		WM	D	0.55	05	13
H	24	WT	D	1.95	328	07
		CC	D	0.11	336	37
		SC	C	2.00	249	47
		CM	D	0.56	189	42
	31	WT	D	2.09	321	20
		FM	C	2.33	70	50
		CC	D	0.28	333	52
		SC	C	0.13	249	48
		CM	D	0.16	197	50
	50	FM	C	0.73	75	63
		CC	C	0.20	334	60
		SC	C	1.47	250	67
		CM	C	0.13	192	63
	21A	WT	D	2.11	356	30
		CM	D	0.31	187	61
		IC	C	0.09	218	54
		FR	D	0.08	133	78
		DM	C	0.14	60	69

Table 4 Continued

Solution	Event Number	Station	First Motion	W_p/W_{s_v}	Azimuth (degrees)	Angle of Incidence (degrees)
I	8	WT	C	2.90	86	48
		FM	C	0.56	85	68
		CC	C	0.33	36	50
		SC	D	0.32	210	36
	9	WT	C	1.94	86	61
		FM	C	1.00	85	77
		CC	C	0.25	32	63
		SC	C	0.32	216	53
		CM	D	0.30	149	71
J	28A	WT	C	1.18	57	55
		CC	C	0.45	18	65
		SC	C	0.46	249	44
		IC	C	0.16	151	41
		WM	C	0.22	124	30
	32A	WT	C	1.33	62	54
		SC	C	0.51	242	47
		CM	C	0.50	148	62
		IC	C	0.13	157	45
		WM	C	0.18	136	34
K	13	WT	D	0.34	359	73
		FM	C	0.39	38	78
		CC	D	0.96	350	79
		SC	C	1.01	299	73

Table 4 Continued

Solution	Event Number	Station	First Motion	W_p/W_{S_V}	Azimuth (degrees)	Angle of Incidence (degrees)
		CM	D	0.73	305	25
	57	WT	D	1.49	03	74
		FM	C	0.31	42	78
		CC	D	1.21	352	78
		SC	C	0.70	298	72
		CM	D	0.74	270	80
L	27A	WT	D	0.42	87	40
		CC	C	0.52	16	52
		SC	C	0.73	228	54
		CM	D	0.72	161	64
		IC	D	0.65	173	54
		WM	D	1.31	168	44
	30A	WT	D	0.63	84	43
		CC	C	0.23	15	55
		SC	C	0.87	230	56
		CM	D	0.71	61	66
		IC	D	0.51	174	55
		WM	D	0.29	168	45
	31A	WT	D	0.39	91	43
		CC	C	0.36	15	55
		SC	C	0.89	228	59
		CM	D	0.61	162	67
		IC	D	0.70	175	58
		WM	D	1.37	171	49

Table 4 Continued

Solution	Event Number	Station	First Motion	W_p/W_{s_v}	Azimuth (degrees)	Angle of Incidence (degrees)
M	20A	WT	D	0.81	298	67
		IC	C	0.02	273	68
		DM	D	1.22	332	59
		TA	D	2.57	331	44
		FR	C	0.36	180	49
	23A	CM	C	0.42	262	87
		DM	D	1.51	326	86
		TA	D	3.00	320	83
		FR	C	0.21	190	84
N	7A	WT	C	0.56	05	60
		SC	C	0.63	283	64
		CM	D	0.77	184	34
		DM	C	0.40	45	74
	15A	WT	C	0.33	14	70
		LD	C	--	348	88
		LPN	C	--	41	88
		SC	C	1.56	276	72
		CM	D	1.89	70	61
		DM	C	1.92	41	81
		TA	C	1.51	72	81
	25A	WT	C	0.40	03	54
		CC	C	0.51	351	69
		SC	C	0.24	280	61
		CM	D	0.95	187	34

Table 4 Continued

Solution	Event Number	Station	First Motion	W_p/W_{s_v}	Azimuth (degrees)	Angle of Incidence (degrees)
		IC	D	1.32	265	32
		WM	D	1.28	303	34

REGIONAL STRESS DISTRIBUTION

A composite fault-plane solution for the entire region near Socorro was constructed using first motion data from 13 of the 14 composite solutions. Solution J was omitted because it was the only solution indicating reverse faulting. The resulting regional composite solution is shown in Figure 30. The solution indicates dominantly normal faulting with a general north - south trend. This result is in good agreement with the tectonics of the Rio Grande rift as described by Sanford et al. (1972) and Chapin and Seager (1975). The dips of both the fault-plane and auxiliary-plane are near 45 degrees. However, normal faults associated with graben structures usually have dips of 55 - 70 degrees. The similarity in dips in Figure 30 could be interpreted as the average dip for fault-planes and auxiliary-planes within the rift. Sanford et al. (1972) showed that the fault movement is not necessarily directed downward toward the central axis of the rift, but that the rift itself is composed of a series of smaller graben and horst structures.

In Figure 31, the orientations of the least (T) and greatest (P) principal stress axes are shown for the 9 preferred solutions and for the regional composite solution. The orientations of the P and T axes indicate crustal extension in an east - west direction.

Although the dominant fault movement has been shown to be normal within the rift, reverse and strike-slip movement (as indicated by the least constrained solutions) may still

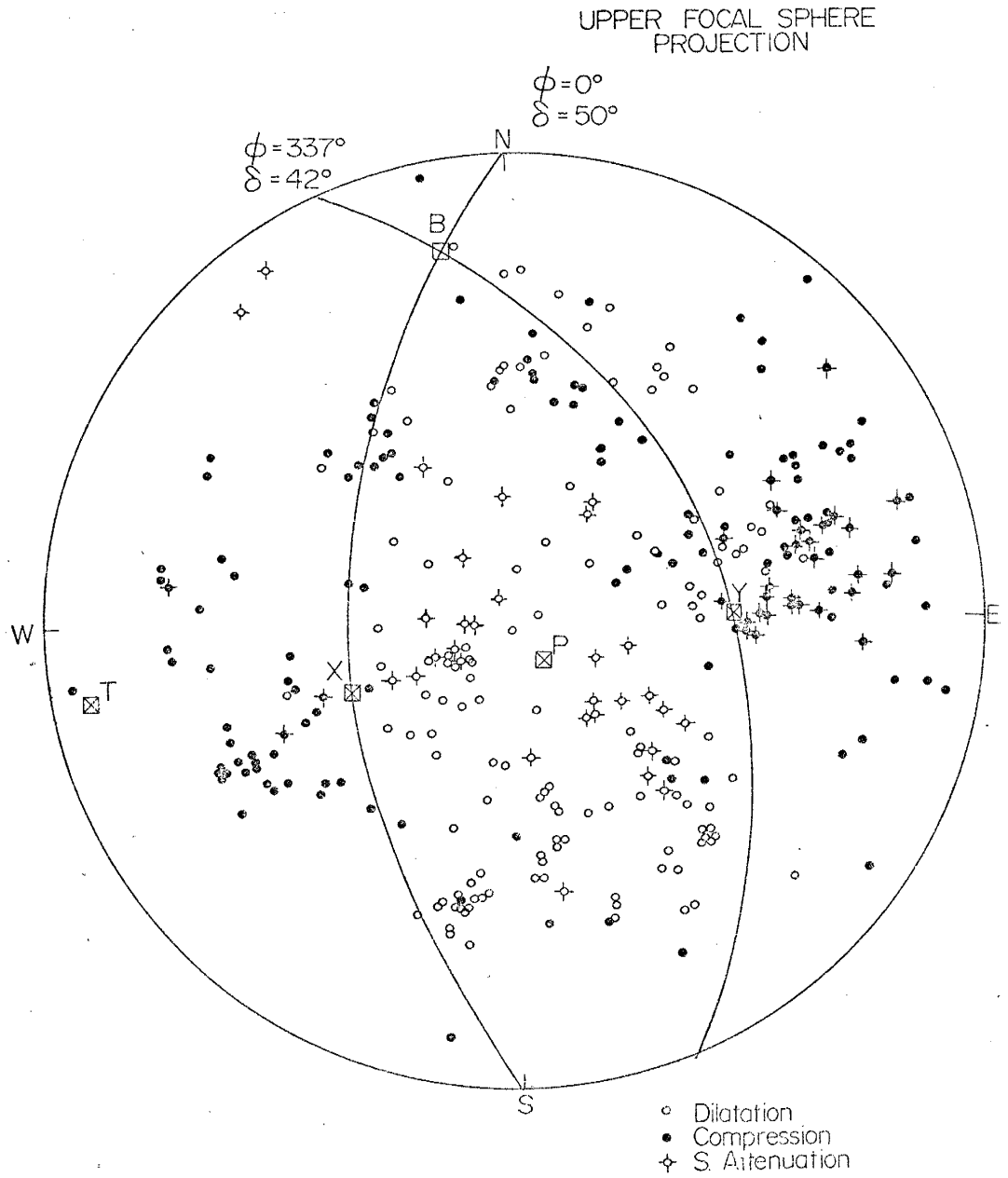

Figure 30 Regional composite fault-plane solution based on first motion data from Solutions A, B, C, D, E, F, G, H, I, K, L, M, N. The solution indicates dominantly normal faulting is occurring in the Socorro region.

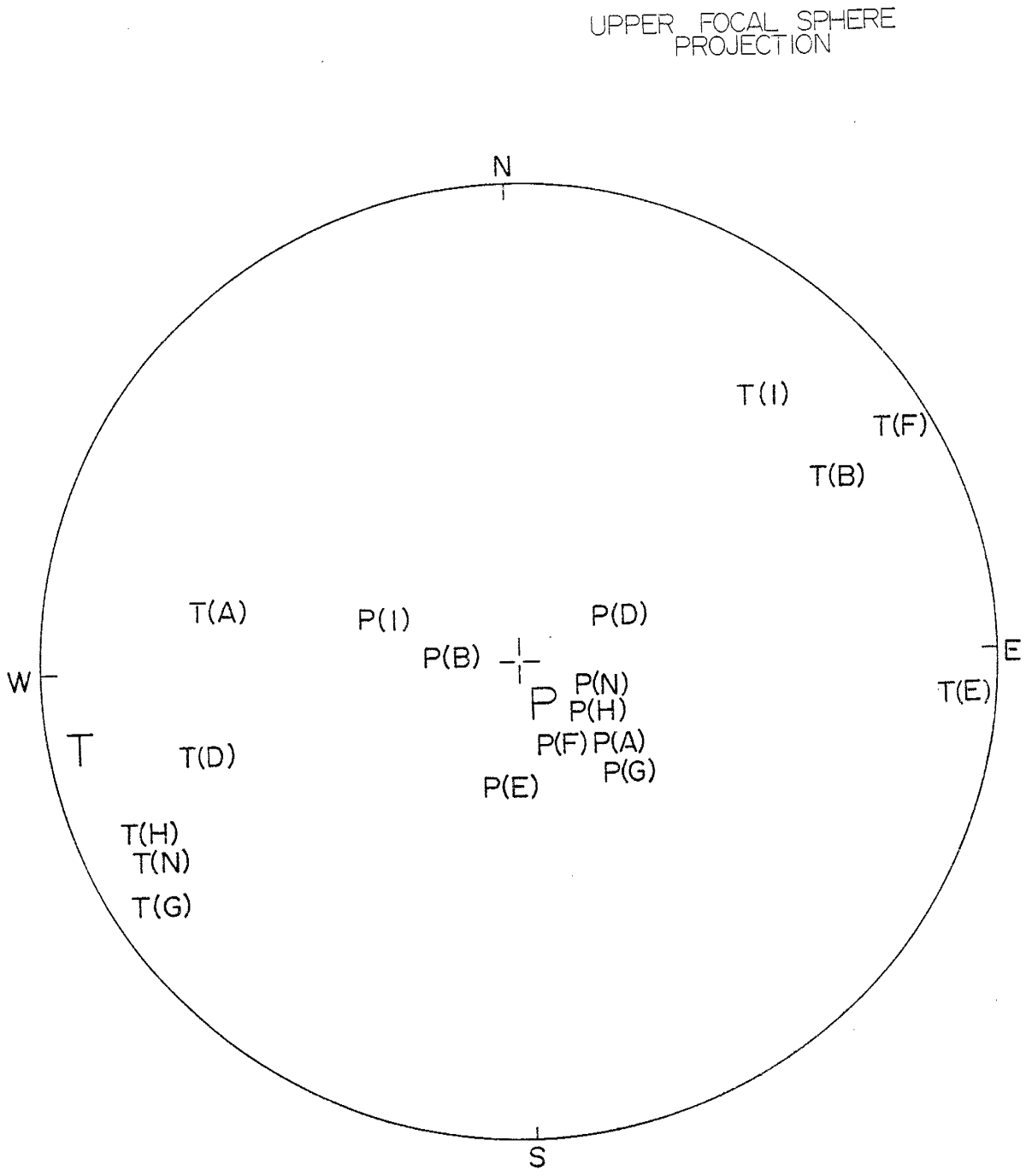

Figure 31 Orientation of the least (T) and greatest (P) principal stress axes for the nine preferred solutions and for the regional composite solution (bold print).

be possible. Such movements could be the result of small localized stress perturbations within the general regional stress distribution.

SHALLOW MAGMA BODIES

S - Phase Screening by Magma Bodies

As discussed in an earlier section, some station recordings of Socorro microearthquakes had unusually small SV amplitudes. Not all of the observations of small SV amplitudes could be explained by the focal mechanism. In this section, the possibility that the observed low SV wave amplitudes could be the result of SV waves passing through molten or partially molten rock (magma bodies) is discussed.

The screening of shear waves has been shown to be a valuable means for detecting the existence of magma bodies in the upper crust (Kubota and Berg (1968), Matumoto (1971)). S phase screening will occur if a magma body lies between an earthquake focus and a recording station. The degree of screening observed will depend upon the following factors:

(1) the polarization of the shear wave; SV waves are more effectively screened then SH waves

(2) the size and shape of the magma body; screening will occur only if the magma body is large compared to the wavelength of the incident wave

(3) the frequency of the incident wave; screening is most effective for high frequency waves .

For a theoretical discussion of S phase screening, see Kubota and Berg (1968).

Other possible explanations must be considered before

attributing the screening of S waves to the existence of a magma body. In addition to focal mechanism, high angles of incidence for SV waves at the free surface could also account for the observed small SV amplitudes. The significance of focal mechanism and angle of incidence, in the interpretation of the Socorro data will be discussed below.

Interpretation of Socorro Results

In order to avoid problems arising from differences in strength of microearthquakes and distances of recording stations, the ratio of the P wave amplitude to the SV wave amplitude, W_p/W_{sv}, was used as a measure of the SV amplitude. High values for this ratio ($1.50 \leq W_p/W_{sv} \leq 8.00$) were observed on microearthquake seismograms recorded at stations FM, WT, SC, CM, IC, WM, DM, and TA.

High angle of incidence of a SV wave at a recording station was investigated as a possible explanation for the small observed SV wave amplitudes. A theoretical curve of W_p/W_{sv} versus D, the linear distance from the epicenter to a recording station, was constructed using the expressions given by Ewing et al. (1957) for incident P and SV waves displacements at a free surface. An average focal depth of 7.0 km, representative of the Socorro area, was used in the calculation of this theoretical curve. It was also assumed that the P and SV waves were of equal strength at the focus, i.e. $W_p/W_{sv} = 1$. Haskell (1964) showed that for shear faulting the S wave amplitude is about 6 times greater than the P wave amplitude at the focus. Because of greater S than

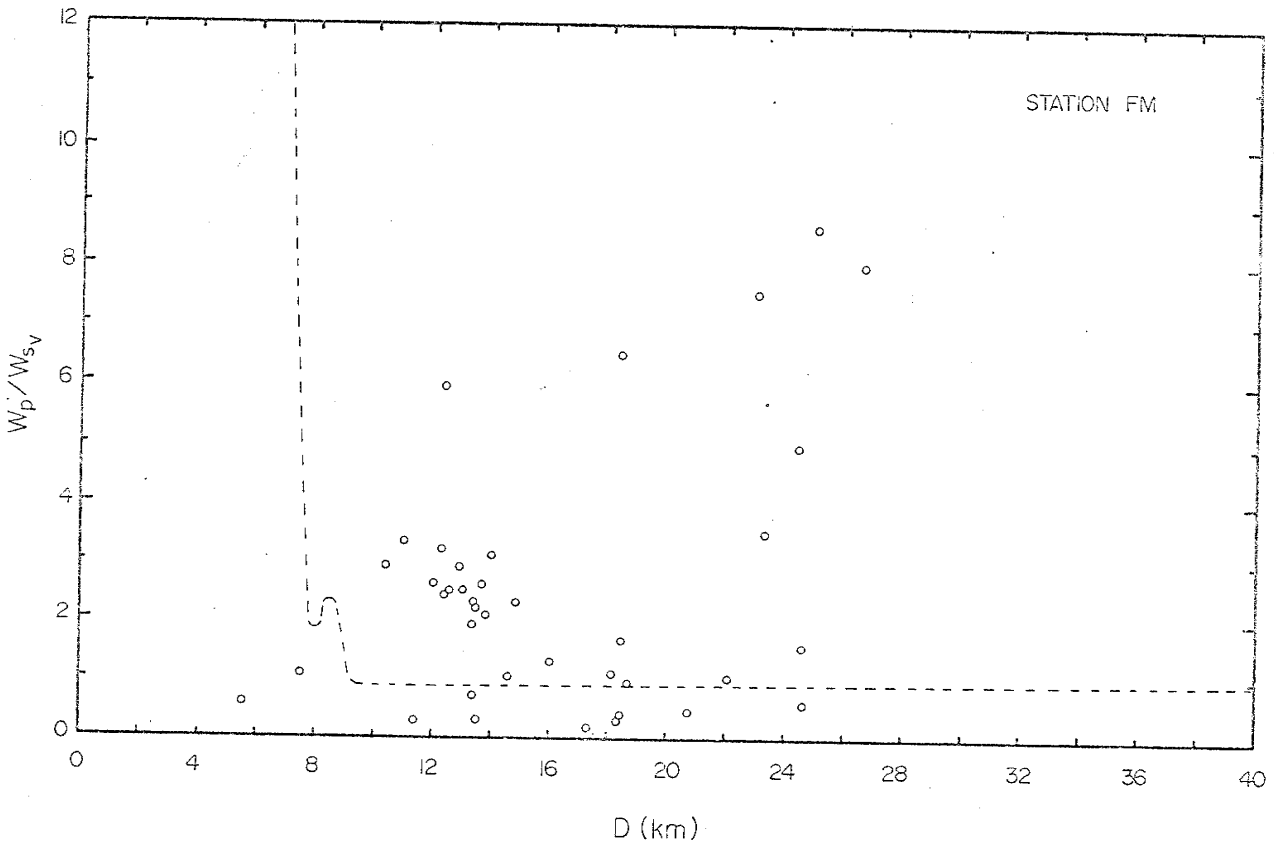

Figure 32 W_p/W_{sv} vs. distance D for station FM. The theoretical curve is shown by the dashed line; the measured W_p/W_{sv} amplitude ratios are shown as open circles. The theoretical curve is based on the assumption that the P and SV waves are of equal strength at the focus.

P wave attenuation, the ratio of S to P at the distance of the recording stations would be substantially less than 6, but still much greater than 1.

In Figure 32, the recorded values of W_p/W_{sv} (open circles) for 39 microearthquakes recorded at station FM are shown with the theoretical curve (dashed line) of W_p/W_{sv} versus distance. The figure indicates that most of the small SV signals recorded at station FM cannot be attributed to a high angle of incidence of SV waves at that station. Similar results, although less extreme, were obtained for data from stations WM, IC, DM, CM, SC, TA and WT.

The possibility that the observed SV wave screening in the Socorro area is a result of the focal mechanism was discussed in the section on Preferred Fault-Plane Solutions. For those solutions, an attempt was made to explain all SV wave amplitudes as indicating the locations of SV nodal planes. However, for 8 of the solutions (Solutions A, H, N, D, F, B, G, E), 62% of the low values observed could not be satisfactorily explained in this way. In these cases, the SV nodal planes do not pass through or very near the points at which the SV waves are absent or very weak (see Figures 21 through 29). Also one of the least constrained solutions, Solution C (Figure 15) shows low SV amplitudes which cannot be explained by any theoretically possible SV nodal plane.

An alternate explanation for the observations would be screening of the SV waves by molten or partially molten bodies (magma bodies) located between the foci of the microearthquakes and the seismograph stations recording the low

SV wave amplitudes. By plotting the raypaths from epicenter to station for those events showing SV wave screening, magma bodies may be assumed to exist where many raypath intersections occur. A restriction on this procedure is that the magma body be located in an area that is aseismic. Temperatures in or very near a magma body would be too high to allow elastic strain energy to accumulate for the generation of earthquakes.

A map showing raypaths along which screening occurs is shown in Figure 33. In Figure 33, only the raypaths for those events showing SV wave screening which could not be explained by SV nodal planes were plotted. As noted before, in the construction of the preferred fault-plane solutions every effort was made to explain the low SV wave amplitudes by the presents of a SV nodal plane. Thus the raypaths shown in Figure 33 represent the minimum amount of SV wave screening by magma bodies in the Socorro area.

All of the SV wave screening shown in Figure 33 can be explained by five elongate magma bodies having a general N - S trend. Possible locations for these magma bodies are (1) an area centered approximately 4.0 km NNE of Socorro within the Socorro basin, (2) an area centered approximately 15.0 km SW of Socorro in the southern end of the La Jencia basin, (3) an area covering most of the Socorro Mountain block including station WF, (4) an area centered approximately 4.0 km SW of Socorro within the Socorro basin and (5) an area centered approximately 12.0 km SSW of Socorro in the northern end of the Chupadera Mountains (see Figure 33). The loca-

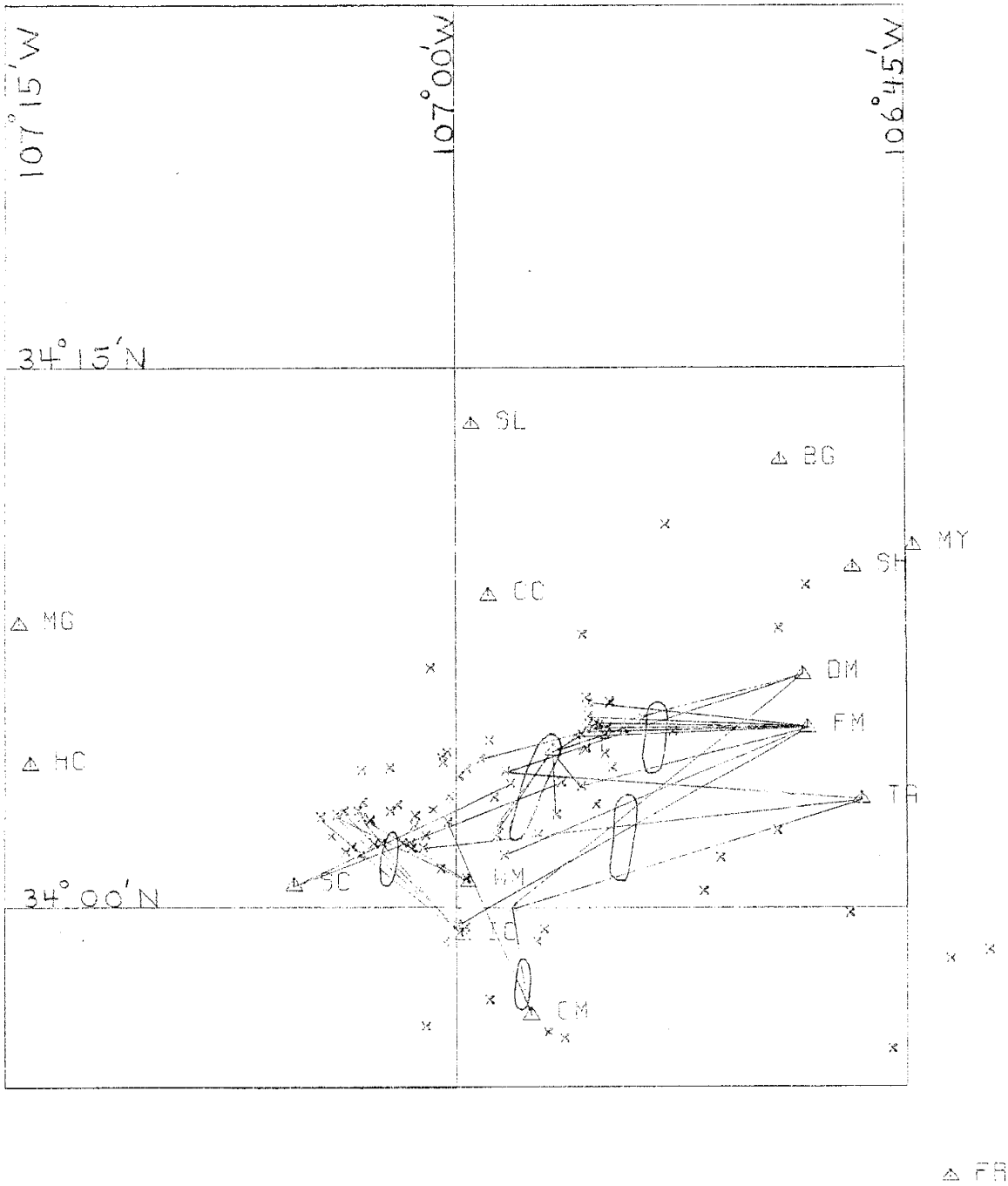

Figure 33 Map showing the locations of five magma bodies in the Socorro area. The locations are based on observed SV wave screening that could not be explained by focal mechanism or high angle of incidence of the SV wave. Raypaths (straight lines) for those events showing SV wave screening are also shown from the epicenter (x) to the recording station (open triangle).

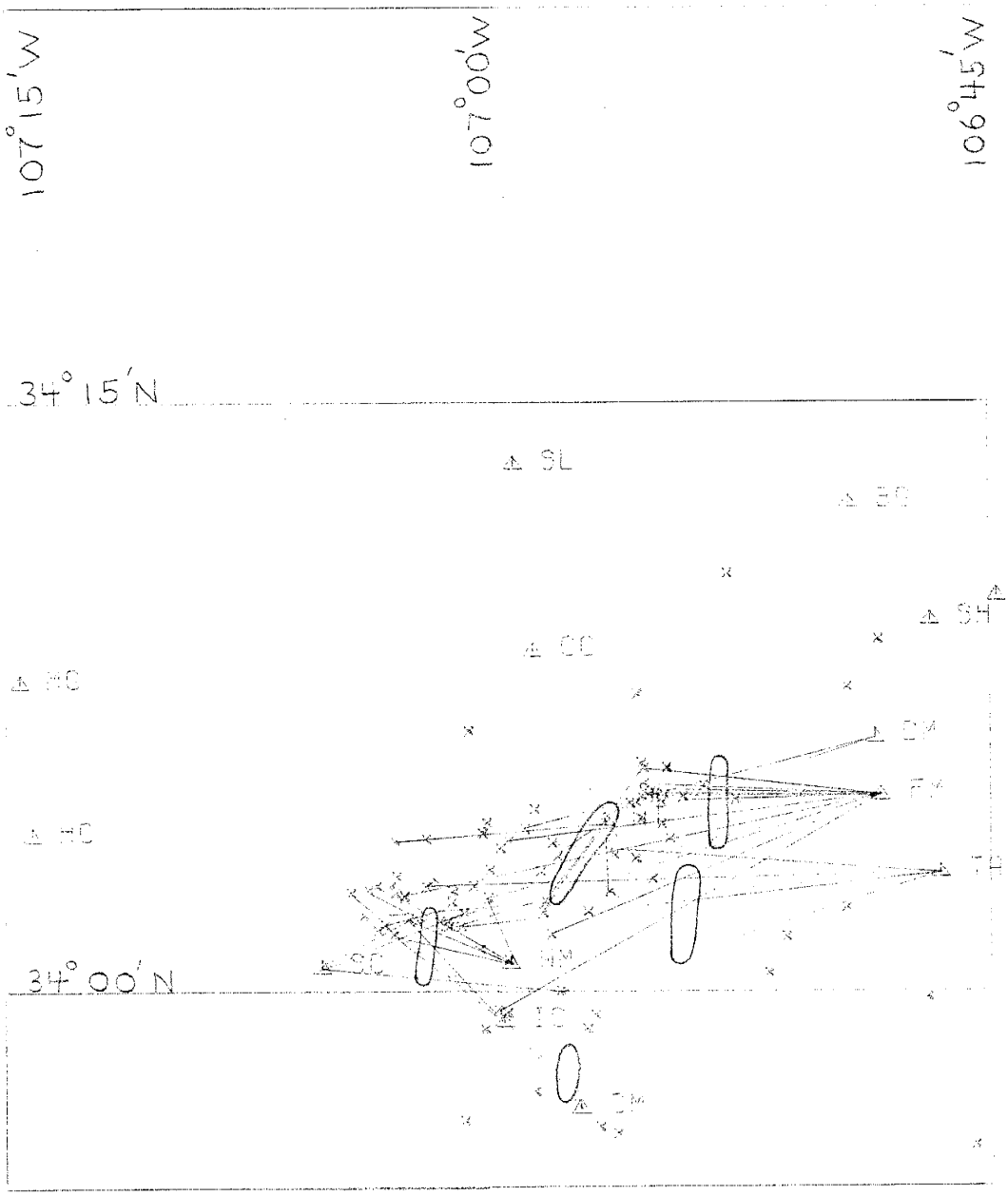

Figure 34. Map showing the locations of five magma bodies in the Socorro area. The locations are based on observed SV wave screening regardless of the screening mechanism. Raypaths (straight lines) for those events showing SV wave screening are also shown from the epicenter (x) to the recording station (open triangle).

tions for these five magma bodies remain the same when ray-paths are plotted for all events showing small SV amplitudes regardless of the cause (Figure 34). Because a majority (63%) of the microearthquake hypocenters in the Socorro area occur at depths between 6.0 and 9.0 km, the maximum depths to the tops of the magma bodies accounting for the observed SV wave screening would be approximately 7.0 km.

SUMMARY

In this study, 69 Class A microearthquakes representing 340 separate seismic events were used to construct a total of 14 composite fault-plane solutions for the Socorro area. Grouping of events for these solutions was based on similarity of first motion and amplitude data. A regional composite fault-plane solution was also constructed using first motion data. Results from the 14 composite solutions and the regional composite solution indicated dominantly normal faulting on fracture surfaces with a general N - S orientation. This result is in good agreement with the tectonics of the Rio Grande rift determined from previous geological and geophysical studies.

For many microearthquakes in the Socorro area, the amplitude and the SV wave was unusually small at one or more stations. Focal mechanism and high angle of incidence for the SV wave were found to be inadequate to explain all of the observed small SV amplitudes. An alternate explanation for many of the observations is that the SV waves were screened during passage through molten or partially molten rock. In all, 5 magma bodies elongated in a general N - S direction are proposed to explain the SV screening. Such bodies would be compatible with the regional stress distribution.

The existence of 5 magma bodies to explain the observed SV wave screening is at this point speculative. The author feels that much more data is needed to confirm their pres-

ence in the Socorro area. Analysis of more microearthquake data following the same methods presented in this paper is required. In addition, the results of this study should be correlated with other seismic research in progress or proposed, such as spacial variations in (1) Poisson's ratio, (2) time residuals for P_g and P_n arrivals, (3) horizontal refractions of P wave arrivals, (4) frequency and amplitude content of P_g arrivals for explosions and regional earthquakes, (5) microearthquake hypocenters, and (6) S_xS reflections from the magma body at a depth of 18 to 21 km.

ACKNOWLEDGMENTS

The author wishes to express his sincere thanks to Dr. Allan R. Sanford for his assistance in all areas of this research and particularly for Dr. Sanford's critical review of this paper. Appreciation is extended to Rick Mott, Eric Rinehart, Frank Caravella, Roger Ward and Terry Wallace for their time spent in data acquisition. The author is indebted to Rick Mott and Eric Rinehart for their work in locating microearthquakes, to Terry Wallace for his computer program helpful in calculating the SV nodal planes and to Dave Bollschweiler for his excellent drafting ability. Particular appreciation is extended to the author's wife for her patience and understanding as well as for her typing abilities.

REFERENCES CITED

Byerly, P. (1938). The earthquake of July 6, 1934; amplitude and first motions, Bull. Seismol. Soc. Amer. 28, 1 - 13.

Byerly, P. (1955). Nature of faulting as deduced from seismograms, Geol. Soc. Amer. Spec. Paper No. 62, 75 - 86.

Chapin, C. E. and W. R. Seager (1975). Evolution of the Rio Grande rift in the Socorro and Las Cruces areas, in New Mexico Geol. Soc. Guidebook, 26th. Field Conf., 297 - 321.

Ewing, W. M., W. S. Jardetzky and F. Press (1957). Elastic Waves in a Layered Media, McGraw-Hill, New York, 374 p.

Gutenberg, B. (1941). Mechanism of faulting in southern California indicated by seismograms, Bull. Seismol. Soc. Amer. 31, 263 - 302.

Hadly, D. and J. Combs (1974). Microearthquake distribution and mechanism of faulting in the Fontana-San Bernardino area of southern California, Bull. Seismol. Soc. Amer. 64, 1477 - 1499.

Haskell, N. A. (1964). Energy of elastic wave radiation, Bull. Seismol. Soc. Amer. 54, 1811 - 1841.

Herrmann, R. B. (1975). A student's guide to the use of P and S wave data for focal mechanism determination, Earthquake Notes 46, 29 - 39.

Hodgson, J. H. and W. G. Milne (1951). Direction of faulting in certain earthquakes of the North Pacific, Bull. Seismol. Soc. Amer. 41, 221 - 242.

Honda, H. (1962). Earthquake mechanism and seismic waves, J. Phys. Earth 10, 1 - 97.

Kubota, A. and E. Berg (1968). Evidence for magma in the Katmai Volcanic range, Bull. Volc. 31, 175 - 214.

Matumoto, T. (1971). Seismic body waves observed in the vicinity of Mt. Katmai Alaska and evidence for the existence of molten chambers, Geol. Soc. Amer. Bull. 82, 2905 - 2920.

Mott, R. P. (1976). The relationship of microearthquake activity to structural geology for the region around Socorro, New Mexico, M. S. Independent Study, Geoscience Dept., New Mexico Inst. Mining and Tech.

Ragan, D. M. (1973). Structural Geology, John Wiley & Sons, Inc., New York, 169 p.

Ramsay, J. G. (1967). Folding and Fracturing of Rocks, McGraw-Hill, New York, 568 p.

Reid, H. F. (1910). The mechanics of the earthquake: the California earthquake of April 18, 1906, Report of the state investigation committee, V. 2, Carnegie Institute of Washington, D. C.

Richter, C. F. (1958). Elementary Seismology, W. H. Freeman and Co., San Francisco, 768 p.

Sanford, A. R. (1963). Seismic activity near Socorro, in New Mexico Geol. Soc. Guidebook, 14th. Field Conf., 146 - 151.

Sanford, A. R. (1968). Gravity survey in central Socorro County, New Mexico, Circ. 91, New Mexico State Bur. Mines Mineral Resources, 14 p.

Sanford, A. R., O. Alptekin, and T. R. Toppozada (1973). Use of reflection phases on microearthquake seismograms to map an unusual discontinuity beneath the Rio Grande rift, Bull. Seismol. Soc. Amer. 63, 2021 - 2034.

Sanford, A. R., A. J. Budding, J. P. Hoffman, O. S. Alptekin, C. A. Rush, and T. R. Toppazada (1972). Seismicity of the Rio Grande rift in New Mexico, Circ. 120, New Mexico State Bur. Mines Mineral Resources, 19 p.

Sanford, A. R. and C. R. Holmes (1962). Microearthquakes near Socorro, New Mexico, Jour. of Geophys. Res. 67, 4449 - 4459.

Sanford, A. R. and L. T. Long (1965). Microearthquake crustal reflections, Bull. Seismol. Soc. Amer. 55, 579 - 586.

Sanford, A. R., R. P. Mott, P. J. Shuleski, E. J. Rinehart, F. J. Caravella, R. M. Ward, and T. C. Wallace (1976). Geophysical evidence for a magma body in the crust in the vicinity of Socorro, New Mexico, Paper Presented at the ONR-CSM Symposium on "The Nature and Physical Properties of the Earth's Crust", Vail, Colorado, Aug. 2 - 6.

Stauder, W. J. (1962). Advances in Geophysics 9, 1 - 76.

Stauder, W. J. and A. Ryall (1967). Spatial distribution and source mechanism of microearthquakes in central Nevada, Bull. Seismol. Soc. Amer. 57, 1317 - 1345.